Title
Architected Materials for Sensing and Actuation

Author
Vella, Gianmarco

Publication Date
2019

UNIVERSITY OF CALIFORNIA SAN DIEGO

Architected Materials for Sensing and Actuation

A thesis submitted in partial satisfaction of the

requirements for the degree Master of Science

in

Materials Science and Engineering

by

Gianmarco Vella

Committee in charge:

Professor Kenneth J. Loh, Chair
Professor Shengqiang Cai
Professor Michael T. Tolley

2019

SIGNATURE PAGE

The Thesis of Gianmarco Vella is approved, and it is acceptable in quality and form for publication on microfilm and electronically:

____

____

____

Chair

University of California San Diego

2019

DEDICATION

To my mother, Mariella, my father, Vincenzo and my sister, Marta.

TABLE OF CONTENTS

LIST OF FIGURES

LIST OF TABLES

ACKNOWLEDGEMENTS

First and foremost, I would like to thank my advisor, Professor Kenneth Loh, a great mentor, teacher and trustworthy friend, both in and outside of the ARMOR Lab. I will always be grateful for the opportunities that Prof. Loh gave me throughout the past years.

Next, I would like to acknowledge two of my collaborators, Sumit Gupta and Yujin Park. Sumit's honest feedback, hard work and guidance throughout the late nights of work have taught me an incredible amount. Chapters 4 and 5 of this thesis report the work done in collaboration with him. The electrical impedance tomography codes and graphene-based conductive ink were developed by Sumit. Similarly, Yujin's patience, friendship and guidance throughout the past year have been essential. Chapter 3 of this of thesis reports the work done in collaboration with Yujin and the code to measure the deformations of the multifunctional active skins was developed by her.

I would also like to extend my biggest gratitude to my ARMOR Lab family. I would have never expected to find such a welcoming, vibrant environment of young, ambitious students that have taught me so much and have become my friends for life. Thank you to Han Joo Lee, Bo Mi Lee, Yun-An Lin, Morgan Funderburk, Tae Hoon Kim, Zachary Huang, Yening Shu, Long Wang and Tian Jiao Zhang. I would also like to thank my colleagues in the Structural Engineering Department: Konstantinos Anagnostopoulos, Gloria Faraone, Margherita Caprotti and Marco Pasetto. Finally, I would like to thank my best friends, for their constant support and love, although being thousands of miles away: Davide Madeddu, Eugenio Maggio and Edoardo Taglione.

Chapter 3 is coauthored with Park, Yujin and Loh, Kenneth J. The thesis author was the primary author of this chapter.

Chapters 4 and 5, in full, are a reprint of the material as it appears in Large Area Distributed Strain Monitoring Using Patterned Nanocomposite Sensing Meshes, Proc. SPIE - Sensors and Smart Structures Technologies for Civil, Mechanical, and Aerospace Systems, 2019. The thesis author was the primary investigator of this paper.

ABSTRACT OF THE THESIS

Architected Materials for Sensing and Actuation

by

Gianmarco Vella

Master of Science in Materials Science and Engineering

University of California San Diego, 2019

Professor Kenneth J. Loh, Chair

The overarching goal of this thesis relies in the exploration of design criteria, such as optimal material layout and geometry, to (1) create and (2) enhance the performance of innovative actuators and sensors, respectively. First, we present a bio-inspired multifunctional active skin, which is a two-dimensional architected material that exhibits local and/or global programmable, rapid, and reversible, out-of-plane surface texture morphing when actuated by in-plane tension. Here, by introducing geometrical imperfection

or notches at judiciously chosen locations in a preconceived, auxetic geometry, we can effectively control the directionality of out-of-plane deformations for applications such as camouflage, surface morphing, and soft robotic grippers.

Second, an innovative “sensing mesh” capable of resolving both spatial strain magnitudes and directionalities for distributed strain field monitoring is introduced. The sensing mesh leverages the same concept of patterning to impart unique sensing capabilities in piezoresistive nanocomposites. In particular, the use of a grid-like layout with high aspect ratio struts resolves the strain sensing directionality limitations observed in previously reported sensing skins while also enhancing the sensitivity of the piezoresistive graphene-based thin films once coupled with an electrical impedance tomography conductivity mapping technique.

Finally, the design considerations explored in this thesis contribute to the development of an inverse design methodology of architected materials in which functionality parameters are first indicated and, then, optimal topologies for maximum effectiveness are indicated.

CHAPTER 1. INTRODUCTION

1.1 Need for Sensing and Actuation

All multicellular living organisms found in nature, except for sponges, placozoans, and mesozoans, show evidence of a nervous system capable of collecting sensory inputs and respond appropriately through motor control. In the human body, the structure of the central nervous system also follows a sensory and motor subdivision. Similarly, today's most advanced engineering systems resemble primitive biological organisms capable of sensing, controlling, and actuating, which is by definition that of a smart structure [1]. There is therefore an emphasis within the scientific community and in the engineering world to further expand the sensing and actuation capabilities for more reliable, responsive, and smart engineered systems.

Sensing technologies play an integral role in each of our daily lives. From measuring our blood pressure throughout the day to air pollution in our cities to chemicals in the soil or water, these applications all rely on the use of sensors. Today's major drivers for sensor applications are centered among challenges related to healthcare, aging population, food/water management, manufacturing, and other pressing environmental issues. Although the large number of fields in which sensors are of key importance, the sensing modalities on which these rely on are few: microelectromechanical systems (MEMS), optical sensors, electrochemical sensors, mechanical sensors, and biosensors [2].

Arguably, in recent years, out of all these sensing modalities, biosensors have become the major driver for innovation in sensing technologies, since this is a potential path for addressing the drastic increase in healthcare costs coupled with the need to deliver better patient care. The shift from reactive to proactive healthcare models relies on personalized health through data collection and tailored interventions ahead of time, making sensors a *sine qua non* for the implementation of such methodologies. Interestingly, the shift to a proactive health monitoring model has extended to engineered structures (*i.e.*, aerospace, civil, and marine) with the only difference that MEMS, mechanical, and optical systems are the predominant sensing technologies encompassed by this exciting field. In structural health monitoring (SHM), the ability to measure, monitor, and assess the health condition of structures has become crucial for the prevention of catastrophic failure and reduction of the extremely high maintenance costs associated with delays in identifying crucial structural issues that have exacerbated over time.

The inputs gathered by the advanced sensing technologies outlined above are of great use only if followed by an actuation response of the engineered system to enhance its performance. The most common actuation modalities of complex engineering systems rely on mechanical and electromechanical actuation to achieve linear motion, rotary motion, or both [3]. More recently, coupling of actuation modalities with innovative materials (*i.e.*, smart materials) expanded the actuation motions achieved [4]. One of the most common and recent examples of engineered systems capable of enhancing performance through a judicious actuation response to sensory inputs is shape-morphing aircraft wings [5, 6]. Additional fields in which shape adaptation as a form of innovative actuation responses that could benefit from this technology are biomedical, automotive, and automation (robotics), to name a few. Interestingly, shape morphing as a form of actuation based on sensory feedback is a skill that nature has perfected throughout billions of years of evolution; the shape morphing of birds' wings for more aerodynamic flying and skin texture change of cephalopods for camouflage, for instance, are clear examples of this [7, 8].

1.2 Background on Architected Materials

In nature, a plethora of examples show evolution-optimized topologies of elemental units that, when replicated in materials, are fundamental to the embedding of functionalities that surpass those inherent to the materials. For example, the porous cellular architecture of beaks in woodpeckers, alternated to dense bone layers, allows for the creation of ordered materials of high stiffness, high strength, low density, outstanding shock absorption, and mechanical energy dissipation capabilities [9-11]. In avian bones and feathers, the porous cellular architecture of the structures and of its cell walls creates a foam-in-foam bone arrangement that is lightweight but of reliable structural integrity [8, 12]. Finally, even in humans, the porosity of the skeleton, varied at discrete sites, allows for lightweight structures with heterogeneous robustness [13]. Yet, although mankind successfully developed materials with properties that go beyond those found in nature, controlling the architecture of elemental units replicated throughout scales is something to be yet explored in depth. Practically, giving an architecture to materials over different length scales corresponds to an additional degree of freedom in the design stage [14].

Humans developed synthetic materials consisting of compounds with chemical compositions and optimized microstructures that overcome the limitations inherent to each material; metal alloys or zirconia ceramics are clear examples of this. However, material properties depend on chemical composition and spatial arrangement of the materials through its matrix [15]. It is by controlling the architecture, rather than the chemical compositions and microstructure alone, that trade-offs inherent to material properties are surpassed, thereby leading to the creation of materials with coupled properties and functionalities (*i.e.,* sensing and actuation).

Specifically, architected materials rely on the careful design of their most elemental unit geometry for coupling of functionalities across length scales. Historically, architected materials were first explored through the design and testing of “metamaterials”. The architecture-driven design of metamaterials has its roots deep in the interaction (and manipulation) of wave phenomena. Metamaterials were first introduced by Jagadish Chandra Bose with his work on the rotation of a polarization plane through his manually fabricated twisted structure [16]. The working principle of optical and acoustic metamaterials relies in the manipulation of waves with wavelengths of equal or larger than that of the architected unit cell making up the metamaterial (typically in the micro- or nano-scale) [17].

In optical metamaterials, both electrical and magnetic fields of light are coupled through the interaction with the “artificial” atoms of the metamaterial, or meta-atoms. Notably, Smith *et al.* [18] first introduced a metamaterial with a negative refractive index, opening up the new exciting field of negative-index metamaterials [19]. Similarly, by exploiting the properties of negative index metamaterials, Pendry [20] first reported the concept of a perfect lens, or superlens, in which a slab of negative refractive metamaterial concentrated all the spectrum of light, effectively being lossless. Despite the controversies raised from this work, the development of superlenses for nanoscale imaging by Taubner *et al.* [21] and of a cloaking metamaterial at microwave frequencies by Schurig *et al.* [22] are few of the many exciting advancements in the field of metamaterials. Simultaneously, acoustic metamaterials, for the manipulation of acoustic and elastic waves, are also a vibrant component of the field of metamaterials. Arguably, of most interest in the field of acoustic metamaterials are phononic crystals and the brilliant applications of phononic bandgaps, which was first reported by Kushwaha *et al.* [23] demonstrating the attenuation of wave propagation in materials [24].

1.3 Architected Materials with Unconventional Mechanical Response: Mechanical Metamaterials

Advances in additive manufacturing (AM) technologies over the last two decades brought a dramatic simplification in the fabrication of materials and structures with complex geometries. At the core of these fabrication techniques is the concept of a "bottom-up" architecture consisting of piecing together smaller material elements to create more complex structures. In conjunction with simplified fabrication methodologies, greater flexibility in the design of three-dimensional (3D) and hierarchical structures led to the development of a new class of architected materials, namely, mechanical metamaterials.

Similar to wave-based metamaterials, the architecture of mechanical metamaterials harvests deformations, stresses, nonlinear responses, instabilities, and mechanical energy in order to achieve desired performances that surpass those of most materials [25]. To be specific, the elemental unit geometries made up of meta-atoms exploit movements (*i.e.*, rotation, buckling, folding, and deformation) in response to external boundary conditions to exhibit, as a collective, the desired behavior. Furthermore, the response to deformation of mechanical metamaterials can be described through four elastic constants: Young's modulus (E), shear modulus (G), bulk modulus (K) and Poisson's ratio (v).

1.3.1 Mechanical Metamaterials: Zero of Negative Poisson's Ratio ($\upsilon \leq 0$ and $G \gg K$)

Most solids exhibit a positive Poisson's ratio; when stretched axially, they contract in a direction orthogonal to the applied load ($\upsilon > 0$). Instead, auxetic mechanical metamaterials ($G \gg K$) expand in a direction orthogonal to that of axial stretching ($\upsilon < 0$). Auxetic materials were first introduced by Evans *et al.* [26] in his work defining and demonstrating synthetic materials exhibiting a negative Poisson's ratio (NPR). The working principle employed by auxetic mechanical metamaterials relies in heterogeneity, as the global response of the material is very different from that of the single unit geometry, with most of its deformations localized at the hinges [25]. In the work by Grima *et al.* [27], rigid rotating squares all interconnected together at their vertices by hinges showed in-plane arrays to provide NPR behavior. By harnessing the heterogeneity of so called "re-entrant" geometries in 3D, Lakes *et al.* [28] first reported a foam-made structure that expanded when stretched. More recently, the versatility of re-entrant geometries was emphasized in the work by Jiang *et al*. [29] who coupled a preconceived re-entrant geometry with a piezoresistive sensor for a 24-fold improvement in sensitivity of the strain sensor.

1.3.2 Mechanical Metamaterials: Negative Compressibility ($-4G/3 < K < 0$)

The response in volume change of solids, when acted upon by simultaneous, uniform pressure, is defined as the reciprocal of bulk modulus ($1/K$), which is compressibility. Most solids show a positive compressibility ($1/K > 0$). Based on the mathematical definition of bulk modulus, the sign of volume change always opposes that of change in pressure [30]. Along the lines of auxetics, negative linear compressibility (NCL) mechanical metamaterials show volume expansion in one direction when acted upon by uniform pressure ($1/K < 0$).

Most importantly, it is the geometries adopted in the design of NLC materials that enable the triggering of this unusual behavior of solids. For example, both “honeycomb” and “wine-rack” configurations are preconceived beam structure networks that are known to exhibit auxetic or NLC behavior only by varying the angles between the connecting beams [31]. Gaedizadeh *et al*. [32] explored two, 3D printed, NLC topologies as reinforcements in composite materials for increasing material stiffness under increasingly applied hydrostatic pressure. Furthermore, by combining NLC architecture and nanotechnology, Aliev *et al*. [33] explored the high-voltage-induced NLC behavior in carbon nanotube (CNT)/aerogel sheets to create artificial muscles with stretch-ability up to 220%. Finally, it is in high pressure environments, such as deep ocean floors, that the versatility of design to trigger NLC behavior could be of great use. For example, fiber optics cables [34] or oil pipelines and platforms are application domains in which NLC architected materials have a lot of potential for innovation.

1.3.3 Mechanical Metamaterials: Tunable Stiffness

The Young’s modulus of solids is an inherent material property unique to its chemical composition and microstructure, among others. Through architecture, flexible mechanical metamaterials enable the tuning of a material’s stiffness on demand, representing a versatile engineering medium for more advanced and responsive engineered structures. Different from most solids in which high density is indicative of high stiffness, architected micro- and nano-lattices like the octet-truss and tetrakaidekahedron enable the creation of ultra-stiff but ultra-light materials. For each of the mentioned lattice configurations, the design criteria derive from the desired deformation mechanism(s). For example, the octet-truss lattice geometry, first introduced by Deshpande *et al*. [35], consists of an octahedron at its core and eight tetrahedrals, each placed on one of the core's faces. All trusses that make up the unit cell have identical aspect ratio. In additional, the forces acting on each of the truss elements are restricted to tension or compression, making the unit cell a stretch-dominated structure. Following similar design criteria, Thomson [36] first introduced the tetrakaidekahedron lattice configuration, which is optimized to fill space while minimizing surface area. The deformation mechanism in the hollow rods that make up the tetrakaidekahedron lattice is bending, making the lattice configuration a bending-dominated geometry. The effectiveness of micro- and nano-lattices for designing materials was demonstrated by Schaedler *et al*. [37] who first introduced metallic (nickel) micro-lattices with a minimum density of 0.9 mg/cm^3. The nickel micro-lattice was capable of full shape recoverability when subjected to uniform, compressive strains up to 50%. Similarly, Bauer *et al*. [38] reported an innovative fabrication methodology for polymer honeycomb micro-lattices that were coated with layers of alumina (Al_3O_2) ceramic through atomic layer deposition (ALD). An increase in the alumina coating layers up to a thickness of 200 nm resulted in a record high strength of 34 MPa for materials with a density regime of 0.7 g/cm^3. More recently, Zhu *et al*. [39] utilized chemical vapor deposition to create 3D graphene aerogel micro-lattices that exhibited compressibility up to applied strains of 90% while also being highly conductive.

1.4 Stiffness Heterogeneities to Harvest Non-linear Responses

The bending stiffness of slender elements increases with the third power of their thickness (with thickness being taken into account in the moment of inertia of the slender elements) [40]. Consequently, building upon heterogeneities in bending stiffness as a new design criterion, mechanical metamaterials with virtually any elastic coefficients can be designed. Coupling of altered bending stiffnesses throughout architected geometries is a recent and exciting field of flexible mechanical metamaterials, especially since induced large deformations and mechanical instabilities lead to nonlinear responses even when the bulk material remains in the linear regime.

1.4.1 Buckling-Induced Instabilities

In nature, the high bending stiffness of slender, beam-like ligaments is what provides structural integrity to avian bones [8]. On the contrary, irreversible deformations of honeycomb structures with ordered, beam-like ligaments proved their effectiveness as collapse bands for applications such as energy absorbing materials [41]. In between null and irreversible deformations, elastic buckling of slender elements due to instabilities is an effective mechanism for reversible and repeatable nonlinear deformations of architected geometries. The work by Mullin *et al.* [42] was among the first ones to demonstrate complete pattern transformation upon applied compression of an elastic sheet with a square array of circular holes. In the elastic sheet array, square elements were interconnected through beam-like ligaments. With applied small loads, the triggered drastic buckling-induced deformations of the beam-like ligaments (hence the nonlinear behavior) showed a new pattern topology, proving the effectiveness of this new design criterion. Harvesting of buckling instabilities of slender beams was also reported by Liu *et al.* [43], where the objective of this study was to show effective negative swelling in materials. Upon exposure to a solvent, the swelling process triggered buckling-induced deformations of the beams into half sinusoid post-buckled configurations. The post-buckled deformations of the beams at discrete locations resulted in a global negative swelling of the interconnected pattern. Moreover, buckling instabilities of slender beams that cause pattern transformation occur over narrow ranges of applied loads. It is therefore possible to create architected materials with tunable properties in which the programmable transformation serves a variety of purposes (*e.g.,* phononic switches, soft robotic locomotion, and robotic propulsion) [44-46].

1.4.2 Bistability

An additional design criterion to harness the nonlinearities in mechanical metamaterials results from the coupling of architecture and bistability of slender beams. In the Euler model, the first stable buckling mode of an elastic beam is obtained when boundary lateral loads are applied [47]. The energy input to the beam (*i.e.,* compressive strain) is dissipated through elastic shape deformation. Once the compressive load is released, the original shape is fully regained, effectively "trapping" the energy induced during deformation [25]. Shan *et al*. [48] reported fully 3D-printable one-, two-, and three-dimensional multistable architectures with beam elements that exhibited controlled bistability once force was applied. Similarly, two stable configurations in post-buckled beams can occur through snap-through instabilities. For beams fabricated with a post-buckled configuration [47], the second stable buckling mode can only appear when extra energy is brought into the system as actuation. Also by Shan *et al.* [48], multistable configurations of the same one-dimensional (1D) architecture of beams was shown to drastically reduce the impact damage effects on an egg attached onto the 1D architected material and released from a predetermined height. In the work by Meza *et al*. [49], hollow beams in the octet-truss nano-lattice configuration were fabricated with an alumina ceramic coating of various thicknesses, which showed local shell buckling that resulted in complete regain of the original shape even when compressed beyond 50% strain. Following the same principles of bistability through actuation, Rafsanjani *et al*. [50] demonstrated a snap-through metamaterial under applied tension. Finally, moving away from energy-trapping implementations, Rafsanjani *et al*. [51]

harnessed snap-through instabilities of beam-like ligaments acting as hinges between rigid squares and triangles to create bistable mechanical metamaterials with auxetic behavior.

1.4.3 Geometrical Frustrations

In flexible metamaterials that show drastic nonlinear behavior, not all deformations are accommodated between neighboring cells, hence creating geometric frustrations within the architecture [52]. An ingenious design criterion relies in the harnessing of geometric frustrations that arise from non-periodicity of design to create programmable metamaterials with a multitude of energy minima [25]. The variety of stable configurations that arise from the ordered, non-periodic, geometrically frustrated designs was shown for its effectiveness for a variety of applications. Celli *et al*. [53] explored geometric frustrations in originally flat, laser-cut, elastic sheets to program out-of-plane shape morphing at discrete domains once point boundary loads were applied. Grima *et al.* [52] demonstrated the effectiveness of quasi-random cuts in elastic sheets to induce geometric frustrations resulting in high auxeticity. Finally, Kang *et al*. [54] explored the design criteria of geometrical frustrations triggered by buckling instabilities in ordered arrays of triangular geometries and tuned the response of the flexible mechanical metamaterial by varying the porosity of the system.

1.5 Research Objectives and Thesis Outline

Based on what was presented in this Chapter so far, architected materials represent a versatile platform for innovative engineered systems. Most importantly, through a variety of design criteria, unique mechanical behaviors of elastic materials can be harnessed and optimized for specific functions. The objective of this thesis was to further explore the effectiveness of new design criteria for the creation of architected materials with applications for actuation and sensing. Chapter 2 provides an overview of the novel fabrication methodologies that have been developed in recent years for the manufacturing of architected materials with complex and exploitable 3D geometries. Building upon the use of advanced fabrication methodologies, Chapter 3 introduces an innovative Multifunctional Active Skin (MAS), which was obtained by harnessing the nonlinear buckling-induced instabilities of a preconceived auxetic geometry simply actuated by in-plane strain. Here, the intent was to demonstrate the effectiveness of a new design criterion based on the judicious placement of geometric imperfections or notches. Then, in Chapter 4, an explanation of electrical impedance tomography (EIT) as a sensing modality for capturing and reconstructing spatial strains (*i.e.*, strain fields) on structural surfaces for SHM applications is discussed. Directly related to EIT, Chapter 5 presents another design criterion based on patterning of a 2D sensing element. Through patterning, a grid-like configuration with high aspect ratio struts was fabricated to solve the limitations in sensing of strain directionality and to enhance the sensitivity of a piezoresistive nanocomposite. The thesis ends with a summary of the work and a discussion of future outlook with the goal of further enhancing the actuation and sensing performance of the MAS and sensing meshes, respectively.

CHAPTER 2. MANUFACTURING PROCESSSES FOR ARCHITECTED MATERIALS

As highlighted in Chapter 1, it is the control over cellular architecture that give mechanical materials properties that go beyond ("meta") those inherent to the materials that constitute them. Hence, of fundamental importance to the field of architected material are processes that do not limit the design freedom and manufacturing feasibility so that higher geometrical complexity often results in more embedded functionalities of metamaterials [14].

Historically, manufacturing technologies have been a major limiting factor for the development of mechanical metamaterials, since only simple unit cell geometries could be manufactured, with the smallest features being in the millimeter scale. In the last two decades, following the advancements in computer aided design (CAD) platforms [55-57], additive manufacturing found applications for a multitude of fields (*e.g.*, robotics, biotechnology, mechanical systems, and materials design). Most importantly, AM brought forth the "bottom up" design concept, based on the addition of materials in a layer-by-layer fashion and giving close to absolute freedom in the design of 3D mechanical metamaterials of complex geometrical configurations. Furthermore, AM enables the manufacturing of architectures over extreme dimensional bandwidths (from nano to macro) in a rapid and simplified manner [58].

2.1 Light-based Manufacturing Processes

Among the many AM processes, light-based ones allow for highest resolution, resulting in the manufacturing feasibility of highly complex designs. The basic principle of light-based AM processes is the shining of a laser onto a bed of liquid, photocurable polymer as feedstock material. Stereolithography (SLA) and two-photon polymerization (2PP) are among the most commonly utilized for the making of mechanical metamaterials due to the high resolutions that both techniques can achieve: approximately 25 μm through SLA [14] and sub-100 nm through 2PP [58]. The differentiating factor between these two AM processes relies in the photon polymerization process of the resin, consisting of a single photon and multi-photon absorption polymerization for SLA and 2PP, respectively [59].

In conventional SLA, a short wavelength laser beam irradiates a bed of resin along the laser "writing" path. Irradiation over the writing path can occur through a mask or directly onto the bed through a set of mirrors that focus the beam at discrete locations. The writing path is computer-generated and consists of sliced cross-sections of the shape being fabricated. Once writing of one layer of the object's cross-section is completed, a thin film of uncured resin is left on it, through either dipping or brushing to which follows writing of the next layer (hence, the layer-by-layer manufacturing approach). It should be mentioned that, in SLA, once the photocurable resin is irradiated, the energy of the laser is greatly attenuated, triggering polymerization only at the surface of the feedstock bed. This results in longer fabrication times, increased cost, and non-homogeneous "stair step" surface finishing, causing a negative effect on the mechanical properties of the fabricated shapes.

The 2PP light-based AM process addresses the limitations of SLA, specifically its speed and resolution, by irradiating a bed of photocurable resin with near-infrared, long wavelength femtosecond laser pulses [59]. The higher energy laser is focused onto the bed of liquid polymer throughout the writing process, triggering polymerization in 3D. It should be mentioned that although the 2PP process still follows a layer-by-layer material curing methodology, all complications associated with the addition of a thin film of uncured resin at each stage of writing in SLA are avoided.

Although restricted to only polymeric materials, the almost unlimited fabrication freedom and high resolution (sub-100 nm) of 2PP fabrication can be coupled with material deposition techniques to create complex metallic and ceramic cellular architectures. In the works by Schaedler *et al.* [37] and Bauer *et al.* [38] reported in Chapter 1, the fabricated polymeric nano-lattices with optimized topologies acted as templates for the deposition of metallic and ceramic thin film coatings through an electroless process and atomic layer deposition, respectively. The polymeric core was then dissolved through chemical etching, leaving freestanding nano-architected (10-100 nm) metallic and ceramic structures, both with record-high material stiffnesses and ultra-low densities. Moreover, as of today, the manufacturing of macro-sized metallic thin films with nano-scale grain size, between 10-20 nm for optimal yield strength, is extremely difficult. The aforementioned highlighted coupling of fabrication (through 2PP) and material coating processes enables the manufacturing of nano-architected geometries with nano-sized grain coatings, which results in exceptionally high mechanical properties of metallic structures [58].

2.2 Extrusion-based Manufacturing Processes

Extrusion-based AM processes were first introduced in the 1980s and also benefitted from the advancements in software platforms capable of virtually slicing objects in a layer-by-layer fashion [55-57]. Fused Deposition Modeling (FDM) is the most widely used extrusion-based AM process today due to its simplicity, cost effectiveness, and satisfactory resolution, thus becoming a key importance for the development of architected materials operating in the micro- to macro-dimensional bandwidth. FDM relies on the melting of thermoplastic filaments that are fed through a heated head and extruded through a nozzle. During printing of each cross-section, the nozzle head extrudes molten material that, by heat transfer, solidifies on top of the previously printed layer. This much simplified printing methodology makes for a fast and cost-efficient technique, with commercially available printers that can run non-stop for days and sold at a wide price range. The work presented in Chapter 3 uniquely relies on FDM that, when coupled with a simple but effective architecture, demonstrated its effectiveness for the fabrication of MAS for programmable and on-demand surface morphing.

It should be mentioned that commercially available FDM printers are bound to nozzle diameters in the range of 0.25 mm, below which these cannot be miniaturized due to complications in the outflow of molten material. Moreover, although light-based processes like SLA suffer from surface finishing defect like “stair steps” in the length scale of 10-100 μm, the low resolution of FDM induces poor surface finish across higher dimensional bandwidths (*i.e.,* millimeter to centimeter). As a consequence, the mechanical properties and deformation mechanisms of FDM printed geometries are highly affected. On the other hand, the material inhomogeneities that affect the deformation mechanisms in mechanical metamaterial geometries can be overcome through additional architecture design criteria, as will be demonstrated in Chapter 3 of this thesis.

2.3 Summary

In the last two decades, exciting progresses have been made in the field of AM. Paramount to this innovative manufacturing branch is the addition, hence the name, of materials in a layer-by-layer fashion to create 3D objects with close to unrestricted geometrical complexity. The design freedom that scientists and engineers now have through

AM has been a key ingredient for the development of architected materials with outstanding and unique functionalities.

AM processes utilized in the field of architected mechanical metamaterials can be divided into light- and extrusion-based. The differentiating factor between the two categories is how the material is added. In light-based processes such as SLA and 2PP, a laser is shined onto/into a bed of liquid, photocurable resin, triggering polymerization and producing layers of material one by one. Light-based AM processes make it possible to manufacture architected lattices of complex topologies across vast dimensional bandwidths (nano- to macro-sized). Commercial SLA apparatuses offer a resolution of ~100 μm with peaks of 25 μm; on the other hand, through 2PP, the fabrication of sub-100 nm architected lattices can be achieved. When coupled with material deposition methodologies (*i.e.,* ALD for ceramics and electroplating for metals), upon etching of the polymeric unit cell acting as a template, freestanding ceramic and metallic nano-architected lattices have been produced (and with record high stiffnesses to density ratios).

The limitations of SLA rely in the layer-by-layer addition of uncured, to then be irradiated, polymeric material. This process is slow and often induces the formation of bubbles or surface inhomogeneities such as "stair steps". On the other hand, as in 2PP, the addition of uncured polymeric material does not occur. Once the laser beam is irradiated into the bath of resin, most parameters (*i.e.,* speed, energy of the laser, and pulses) regulating the printing process are very much experimental, hence making the printing process non-trivial. Moreover, exposure of the resin bath to humidity might cause inhomogeneities in the printed component, especially when dealing with nano- to micro-sized components.

CHAPTER 3. MULTIFUNCTIONAL ACTIVE SKINS FOR SURFACE MORPHING

3.1 Introduction

Chapter 1 presented a vast variety of mechanical metamaterials that adopt a multitude of design criteria (*e.g.*, geometric heterogeneities, stretch- and bending-dominated structures, elastic-buckling of beams, and geometric frustrations) to leverage precise geometric designs and imperfections to induce unique material behavior. Simultaneously, with the advancement of additive manufacturing technologies, light- and extrusion-based processing techniques brought a dramatic simplification in the fabrication of materials with complex geometries, which was presented in Chapter 2.

In this chapter, the simplicity of AM extrusion-based FDM 3D printing was combined to the design criterion based on the introduction of hinge-like notches or instabilities throughout a preconceived auxetic geometry to produce a new class of instability-induced morphable structures. The proposed MAS is a bio-inspired, 2D architected material that exhibits local and/or global programmable, rapid, and reversible, out-of-plane surface texture morphing when actuated by in-plane tension. By introducing instabilities or notches at judiciously chosen locations within the unit cell, the directionality of out-of-plane deformations can be effectively controlled, demonstrating a broad possibility of applications (*e.g.*, camouflage and small- to large-area gripping).

The motivation for investigating this architected actuation response comes from nature, as some of its creatures can dynamically morph their skin texture to adapt to their ever-changing surroundings. Coleoid cephalopods, namely octopus and cuttlefish, are capable of changing their skin from a smooth to a jagged texture, on-demand and reversibly, for signaling, hunting, and camouflage [60]. In cuttlefish, both the concentric and horizontal erector muscles, which exist in the initially smooth 2D soft-tissue, contract at discrete locations throughout the cephalopod's skin to exhibit protruding 3D surface "bumps" or papillae (Figure 3.1A-C). This ingenious ability of cephalopods to continuously morph their surface texture is direct evidence that their skin is active and multifunctional.

Moreover, these unique morphing skins found in nature have motivated studies focused on designing and architecting bio-inspired materials that exhibit functionalities such as auxetic behavior [61-63], enhanced stretch-ability [64], negative thermal expansion [65, 66], and swelling properties [43, 67]. A common mechanism that these carefully structured materials leverage is to excite instabilities within the structure to generate the desired functionalities. More recently, simple harnessing of instabilities through carefully perforated elastic sheets demonstrated its effectiveness as a mechanism for controllable friction properties of a surface [45]. Such architected materials, for example, linear-elastic materials that display non-linear response, can be employed for designing robots [68], actuators [69], stretchable electronic devices [70], and shape morphing sheets [53, 71].

3.2 Results

3.2.1 MAS unit cell geometry

The star-shape geometry of our MAS (Figure 3.1D) is a modified version of a preconceived geometry, which was first reported as part of re-entrant cell geometries displaying a negative Poisson's ratio [28]. Due to its simple geometrical configuration and auxetic behavior, it was adopted as static inclusions for modeling fiber-reinforced honeycomb composites [72], as well as in dynamic studies for wave propagation [73], band gap [74], and acoustic super-lens design [75]. Yet, to the best of our knowledge, no

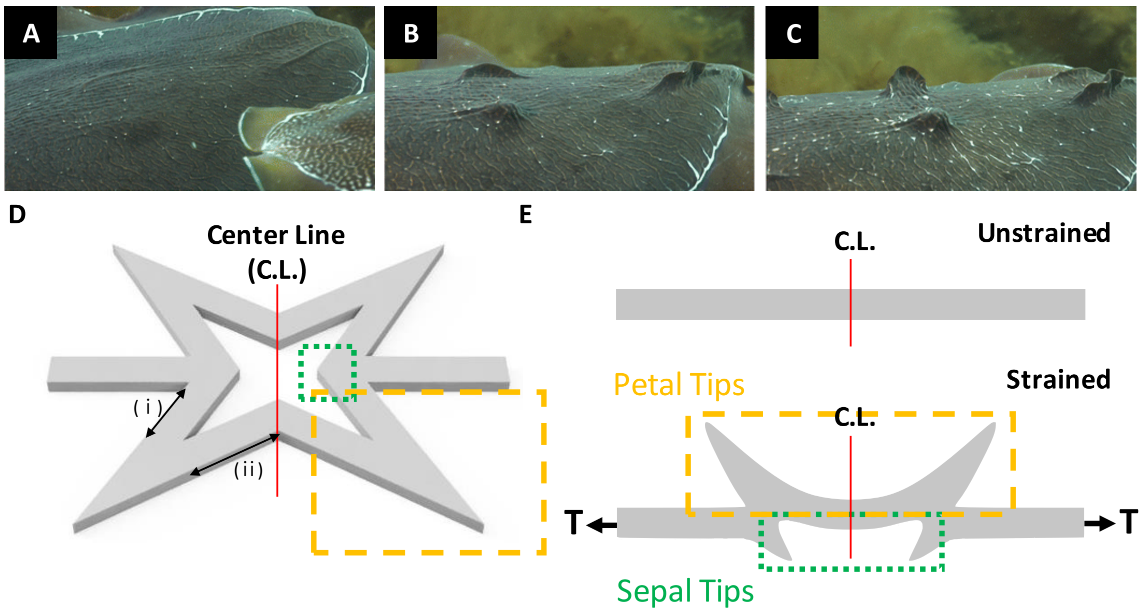

Figure 3.1. (**A-C**) The *Sepia Officinalis* displays dynamic skin texture morphing (2D to 3D) from smooth to partially expressed to fully expressed papillae. Skin texture transformation through papillae expression takes approximately 2 s. Figures are reprinted by permission from Springer Customer Service Centre GmbH: Springer, Journal of Comparative Physiology A: Cuttlefish use visual cues to control three-dimensional skin papillae for camouflage, Justine Allen, Lydia M. Mäthger, Alexandra Barbosa, Roget T. Hanlon, COPYRIGHT (2009) (**D**) A rendering (slanted view) of the MAS star geometry with the box showing one of the "arms" of the star geometry is presented. (**E**) The side view of the two MAS star geometry configurations is illustrated. In the unstrained condition, the star geometry is flat. Under uniaxial strain, buckling-induced instabilities of the MAS star geometry trigger out-of-plane shape morphing of jagged features, resembling that of the papillae found in coleoid cephalopods.

investigations on harnessing the load-induced mechanical instabilities produced by the star-shaped geometry have been reported.

Interestingly, the star geometry exhibits mechanical instabilities triggered by uniaxial tension when replicated as an originally flat, elastic substrate below a certain threshold thickness. The geometry undergoes reversible shape morphing with each of the four "arms" of the star (Figure 3.1D) protruding out-of-plane when acted upon by uniaxial tension (Figure 3.1E). For simplification, in the deformed state, a distinction is made between star geometry arms (calling these petal tips, which are boxed in yellow in Figure 3.1E) and the arrowhead-like tips at the inner junction of two adjacent arms (calling these sepal tips, which are boxed in green). Furthermore, when the star unit cells are interconnected to form arrays, discrete out-of-plane surface morphing of each unit results in global texture morphing of the surface with resemblance to that of cephalopods.

3.2.2 Deformation mechanism of MAS

The stress-strain deformation mechanism of a single MAS star geometry with 1.0 mm substrate thickness under uniaxial tensile loading is depicted in Figure 3.2. Unlike a typical stress-strain curve, where elastic deformation (linear) is uniform and is rapidly followed by plastic deformation (non-linear), the elastic deformation region exhibited by the star geometry appears to be more intricate and segmented (Figure 3.2B). The distances between sepal (DBS) and petal tips (DBP) post-buckling are measured for characterizing MAS behavior and are presented as a performance indicator in Figure 3.2C. To further elucidate the mechanisms responsible for deformation, Figure 3.2D present the mechanical response of a unit cell under different magnitudes of applied tensile strains.

In the initial stage of elastic loading (*i.e.,* orange-shaded region delimited by points O-I in Figure 3.2B and 2D), the deformation of the MAS star pattern remains in-plane. During elastic loading, the ends of the sepal tips move in parallel with the direction of applied tensile strains until θ_1 reaches 90º.

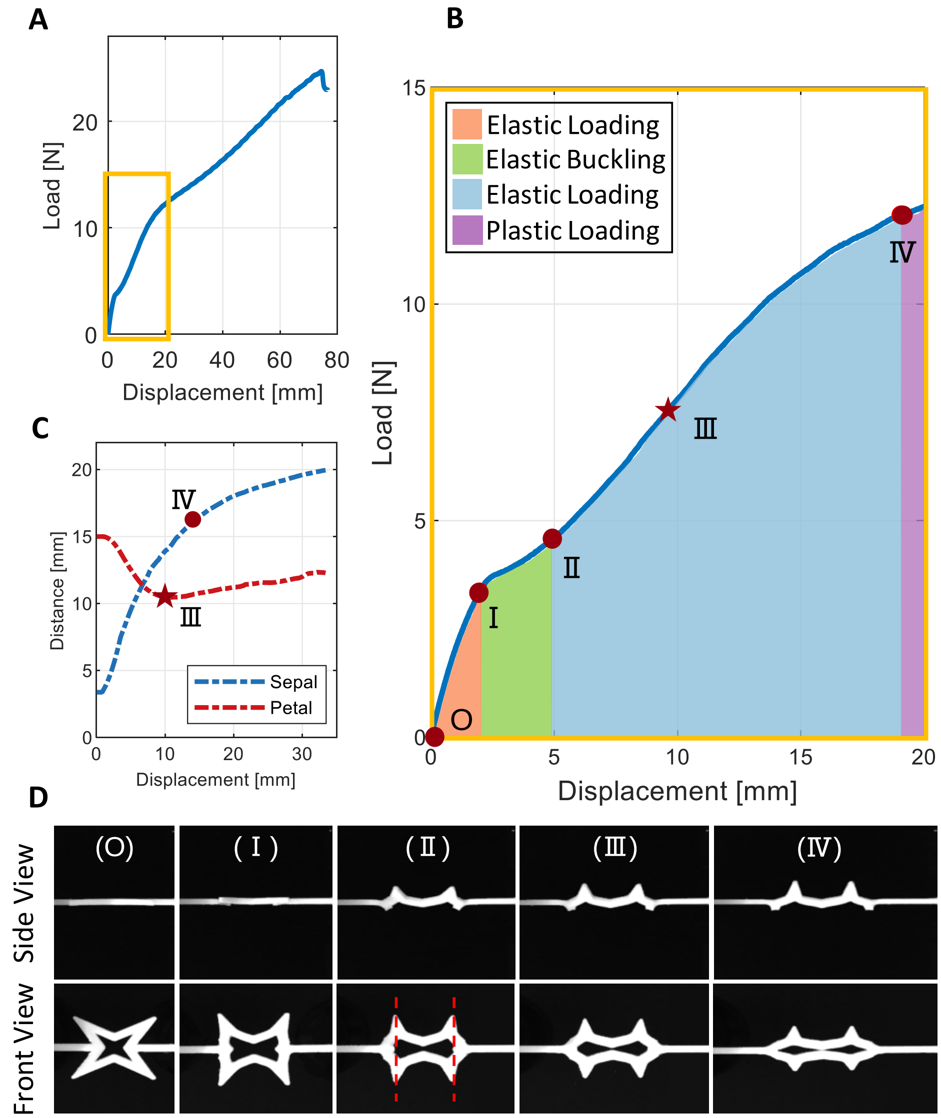

Figure 3.2. (**A**) The load-displacement curve of a 1.0 mm thick unit MAS star geometry under uniaxial tension is plotted. (**B**) The elastic deformation zone of the MAS star geometry is highlighted. Each deformation region is segmented through regression analysis, and points corresponding to changes in MAS behavior are marked. (**C**) The distances between petal tips and sepal tips throughout the deformation of a unit MAS star geometry is plotted. Petal tips keep moving towards each other until point III, which is the minimum distance between petal tips. Point III is also marked in Figure 3.2B (**D**) Visual insight of the deformation behavior of the unit MAS star geometry at each of the points of interest (from O to IV) is presented using video collected during experimental testing.

Following elastic loading, the stress-strain curve transitions to become highly non-linear (green-shaded region in Figure 3.2B). Effectively, point I corresponds to the critical buckling point of the star geometry as it delineates the start of out-of-plane buckling of the sepal and petal tips. Continued applied uniaxial tension induces outward movements of the sepal tips and results in localized compressive stresses in the angled lateral elements meeting at the sepal tip (Figure 3.2D(I)). These compressive stresses induce out-of-plane buckling and emulates a seesaw-like behavior of the petal and sepal tips. Effectively, sepal tips are always pushed in the direction opposite to that of the out-of-plane deformation of the petal tips to accommodate the new equilibrium configuration of the MAS star geometry. Non-linear behavior ends when the ends of the sepal tips and petal tips are aligned in Figure 3.2D(II).

Thereafter, the stress-strain curve regains linearity (blue-shaded region in Figure 3.2B), since buckling has occurred and that there is no additional out-of-plane movement. From points (II) to (III) in Figure 3.2D, the seesaw-like behavior enlarged the gathering of the petal tips, where this response is only governed by the elongation of the MAS side supporting beams (Figure 3.1D(ii)). Thus, DBP reaches the minimum at point (III), indicating full out-of-plane deformation or deployment of the geometry as shown in Figure 3.2C. After point (III), the seesaw-like behavior is attenuated, and the petal tips move away from one another like the sepal tips. When the curve reaches point (IV), plastic deformation occurs (*i.e.,* purple-shaded region in Figure 3.2B).

3.2.3 Mechanical performance of MAS

Figure 3.3A captures the mechanical behavior of the MAS star geometry and the effects of different thicknesses under applied uniaxial tension. As substrate thickness decreases, Figure 3.3B shows that the critical buckling point or the initiation of out-of-plane shape morphing shifts leftwards and downwards along each line. Otherwise, the initial stress-strain responses of different thickness MAS stars superimpose and are governed by the linear-elastic response of the material used. Since critical buckling load is linearly proportional to bending stiffness and decreases as the thickness of the substrate is reduced, there is an energetical benefit in using lower substrate thicknesses as this results in lower applied uniaxial tension to start and attain full out-of-plane shape morphing. Figure 3.3C also confirms that DBP changes more dramatically when star thickness and bending stiffness are reduced.

In theory, the buckling-induced, out-of-plane, shape morphing orientations of the star geometries are highly dependent on load perturbations and material inhomogeneities regardless of their thickness. Despite the advantages of reducing bending stiffness, 3D-printing of star geometries on thinner substrates make them even more susceptible to process-related phenomena and material inhomogeneities. This effect is witnessed during our experimental study, where 0.5 and 1.0 mm thick star geometries produce random, out-of-plane, petal tip deformation directions (Figure 3.3D-E).

3.2.4 Programmable MAS through imperfections

As a means to control and harness the buckling-induced instabilities of the MAS star geometry, geometrical imperfections or notches are introduced at key locations throughout the structure. These notches shift the neutral axis locally and asymmetrically, thereby forcing out-of-plane deformations to occur in a deterministic and programmable direction. Such purposefully designed geometrical imperfections overpower the undesirable effects of material inhomogeneities to enable directional control of out-of-plane buckling induced deformations.

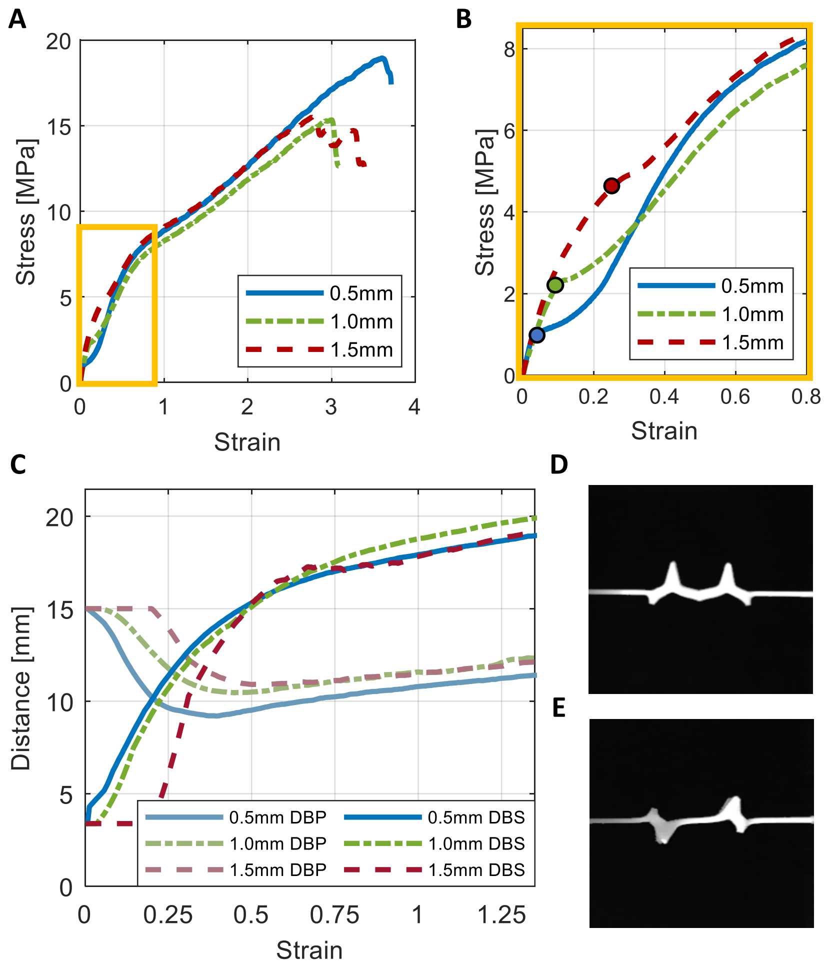

Figure 3.3. (**A**) Uniaxial stress-strain responses of the star geometry with 0.5, 1.0, and 1.5 mm substrate thicknesses are overlaid. (**B**) The elastic deformation zone of the stress-strain curve (yellow box in A) is highlighted. The critical buckling point for each star geometry is also marked. The curves diverge after the critical buckling point and then overlay each other once elastic buckling has occurred. (**C**) The measured distances between petal (DBP) and sepal (DBS) tips throughout the entire deformation process are overlaid. DBP and DBS in the initial or pristine state of MAS is 15 mm and 3.38 mm, respectively. (**D-E**) Unidirectional and random out-of-plane buckled configurations of the star geometry under uniaxial applied strain are observed during testing.

Therefore, geometrical imperfections were judiciously placed at the start/end of each arm of the star geometry as shown in Figure 3.4A-B. Four notches, as shown in Figure 3.4A(iii), are introduced at the base of the sepal tips. Applied in-plane tension to the supporting beams (Figure 3.4A(ii)) results in compressive stresses in arms with notches and ultimately localized buckling around Figure 3.4A(iii). In addition, four additional notches (Figure 3.4A(iv)) are located next to the petal tips. As applied tension induces separation of the sepal tips and the buildup of internal bending moments near notches shown in Figure 3.4A(iii), the notches at Figure 3.4A(iv) drive out-of-plane deformations of the petal tips to maintain static equilibrium.

The effect of notch geometrical design (with three normalized depth of h/t = 1/3, 1/2, and 2/3 while fixing width, w = 1.0 mm) on the mechanical behavior of the MAS star geometry was also investigated. The stress-strain response of a 0.5 mm thick star geometry is directly compared to its respective unnotched (h/t = 0) configuration (Figure 3.4C-E). The introduction of the mid-depth notch (h/t = 1/2) resulted in a reduced critical buckling stress (or load) by ~ 40% (Figure 3.4C). Increasing normalized depths of the notches further decreased critical buckling load (Figure 3.4C) while improving out-of-plane deformations of the star geometry, which is quantified by DBP (Figure 3.4D). As expected, the notched star geometry with h/t = 2/3 resulted in the greatest petal tip deformation at the least amount of tensile stresses applied. It should be mentioned that in the 0.5 mm thick star geometry, introduction of the shallowest notch (h/t = 1/3) did not show an effective reduction of the critical buckling load. It is believed that at such low notch depths, the fabrication accuracy is not high enough to induce an effective shift downward of the neutral axis. Hence, fabrication defects still prevail over the deformation mechanism of the star geometry, showing a stress-strain response that matches that of its respective unnotched (h/t = 0) configuration (Figure 3.4C).

3.2.5 Reversibility of MAS

Buckling of materials in the elastic domain is reversible and repeatable. To study the reversibility of MAS, the star geometry was tested under displacement-controlled tensile cyclic loading. The unit cell star geometry was cyclically strained from 0 to approximately

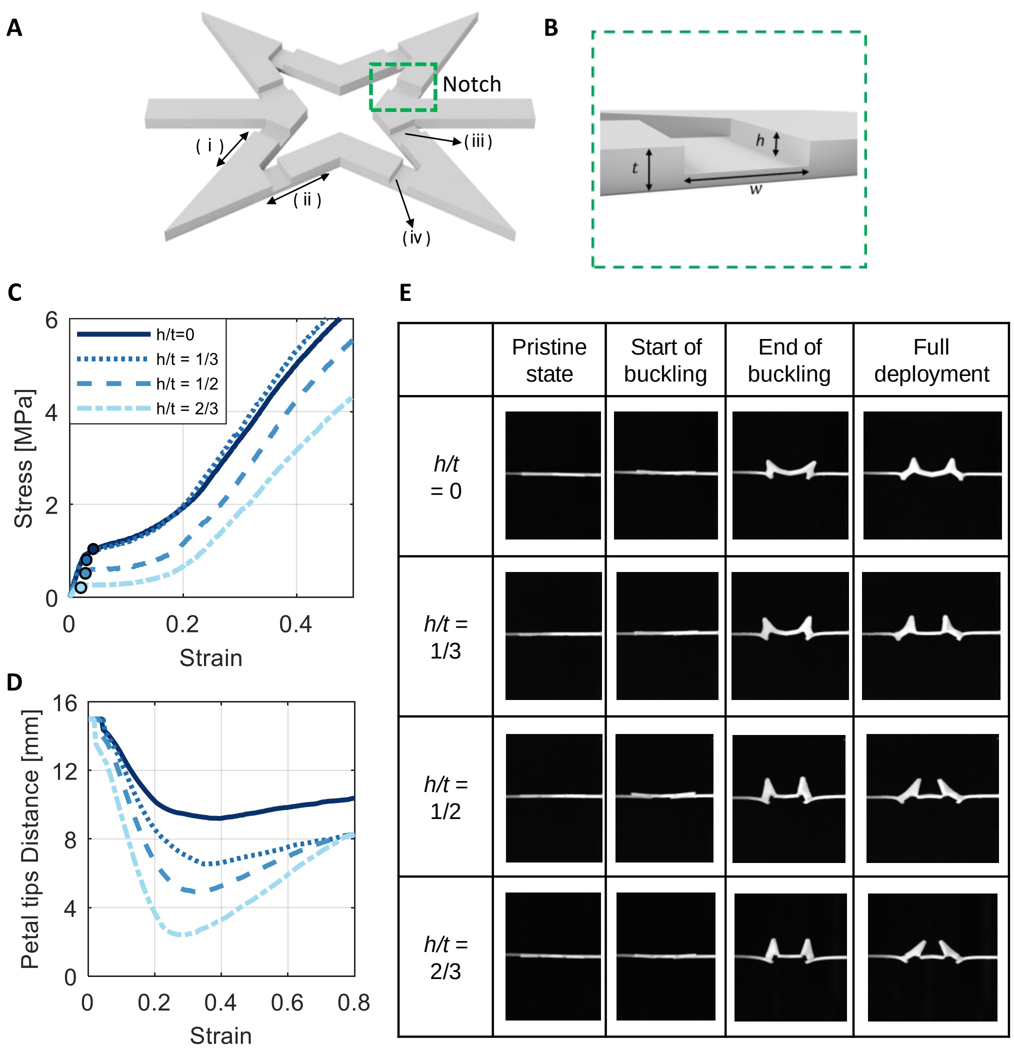

Figure 3.4. (**A**) A rendering of the notched MAS unit star geometry is shown, where (i) and (ii) represent the beams of the MAS that meet at the sepal tips and supporting beam, respectively. (iii) and (iv) are the notches induced to control buckling direction and maintain static equilibrium. (**B**) The thickness, *t*, depth, *h,* and width, *w* of notches in the MAS geometry are illustrated. (**C**) The mechanical response of notched MAS for *h/t* = 1/3, 1/2 and 2/3 are overlaid. (**D**) The measured distance between petal tips (DBP) throughout the deformation are plotted. (**E**) Picture frames extracted from video taken during tensile testing of the unit notched MAS star geometry shows its deformation behavior at each of the points of interest (from 0 to III in the deformation mechanism).

minimum DBP (*i.e.,* equivalent to point III in Figure 3.2B) to attain full MAS deployment. All tensile tests cyclic were conducted using specimens 1.0 mm thick and $h/t = 2/3$. Figure 3.5A overlays the stress-strain responses of a representative specimen subjected to tensile cyclic tests. First, the stress-strain response of the 1st cycle is consistent with results presented earlier in Figure 3.4C. Evidence of slight plastic deformation and/or creep is seen in this case, where compressive stresses are induced to return the specimen back to its pristine state.

Second, the next five cycles of loading (2nd to 6th) suggest stress-softening of the star geometry, where maximum stress at peak tensile strain decreases progressively with each additional cycle of loading. Finally, a stabilized hysteresis loop is obtained after six loading cycles. Figure 3.5B illustrates the decrease in applied load to attain full deployment of the notched 1.0 mm thick MAS star pattern following cyclic loading. Despite the change in its stress-strain response, out-of-plane deformation behavior post-cyclic loading is comparable to its pristine (non-cycled) specimen as shown in Figure 3.5C, thus clearly highlighting the reversibility and repeatability of the shape morphing properties of the MAS star geometry. Overall, out-of-plane deformation is triggered by applying low magnitudes of strain, and the MAS can respond to sudden applied strains and in a controlled manner [76].

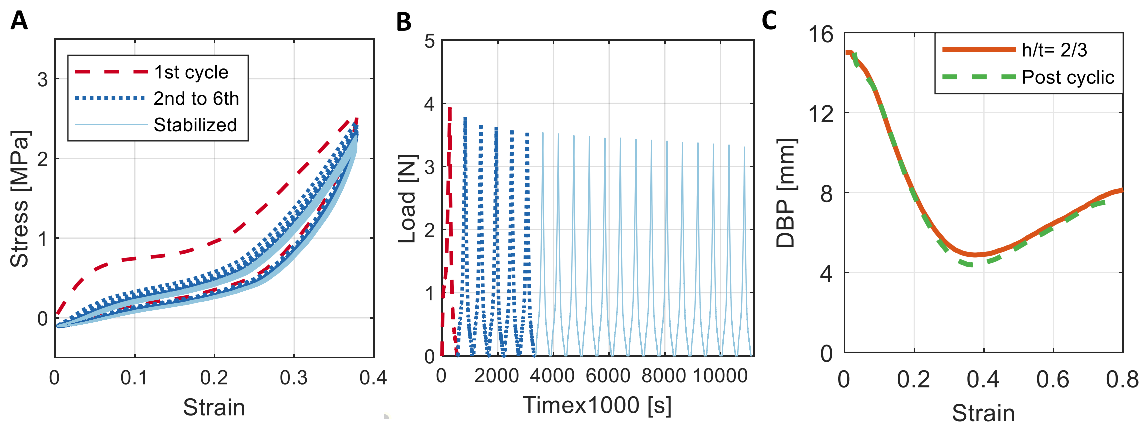

Figure 3.5. (**A**) Stress-strain hysteresis curves are obtained during tensile cyclic tests. (**B**) The plot shows the applied cyclic load time history necessary to attain full MAS deployment. (**C**) DBP plots corresponding to the first cycle of tensile loading and post-cyclic testing show comparable behavior.

3.2.6 Versatility of MAS

The versatility of the methodology for harnessing mechanical instabilities through geometrical imperfections presented thus far is shown in Figure 3.6. Including, omitting, or alternating the placement of notch designs throughout arrays of 3D-printed star geometries can yield MAS prototypes intended for different functionalities. First, a 7×7 array of interconnected star geometries was designed and printed to display programmable and localized actuation (Figure 3.6A). During array design, stars highlighted in red were notched, while all others were unnotched. Uniform, uniaxial tension was applied to stretch the array in the vertical direction while keeping the bottom fixed. Because unnotched stars require larger strains to induce out-of-plane deformations, the induced strains acting on the programmed MAS resulted in controlled shape morphing to display an embedded "1 2 3" pattern (Figure 3.6A). It should be mentioned that the alternation of notched to unnotched star geometries for successfully displaying an embedded pattern is only valid up until the critical buckling load of the unnotched star geometries. Further straining the array would deploy the entire MAS pattern.

Next, the out-of-plane shape morphing behavior of star geometries was harnessed for gripping. A 5×5 MAS array of interconnected notched stars throughout the entire array was 3D-printed and demonstrated for large-area gripping (Figure 3.6B). The MAS was placed over randomly distributed fur balls (~ 1 g each) and then stretched manually to engage the star grippers for grabbing multiple objects at once. Unique to using MAS for gripping is the use of in-plane tension as the actuation mechanism. This is in contrast to most grippers that require the direct application of compressive forces on two opposing surfaces (or fingers) to restrict the motion of an object trapped in between. One can observe in Figure 3.6B that some stars folded in a random (or incorrect) direction despite the use of notched stars. It should be clarified that this was a result of manually stretching the star array, where rotations and nonuniform tensile strains were inadvertently applied.

Last, the coupling of an accordion-like, soft, linear actuator with a MAS star on opposite faces enabled the creation of a soft robotic claw crane (Figure 3.6C) [77]. Pneumatically actuating the soft accordion caused it to extend horizontally, thereby applying uniform tensile strains to the MAS and triggering out-of-plane folding of the star arms. An additional linear accordion actuator was connected perpendicular to the "soft claw" for

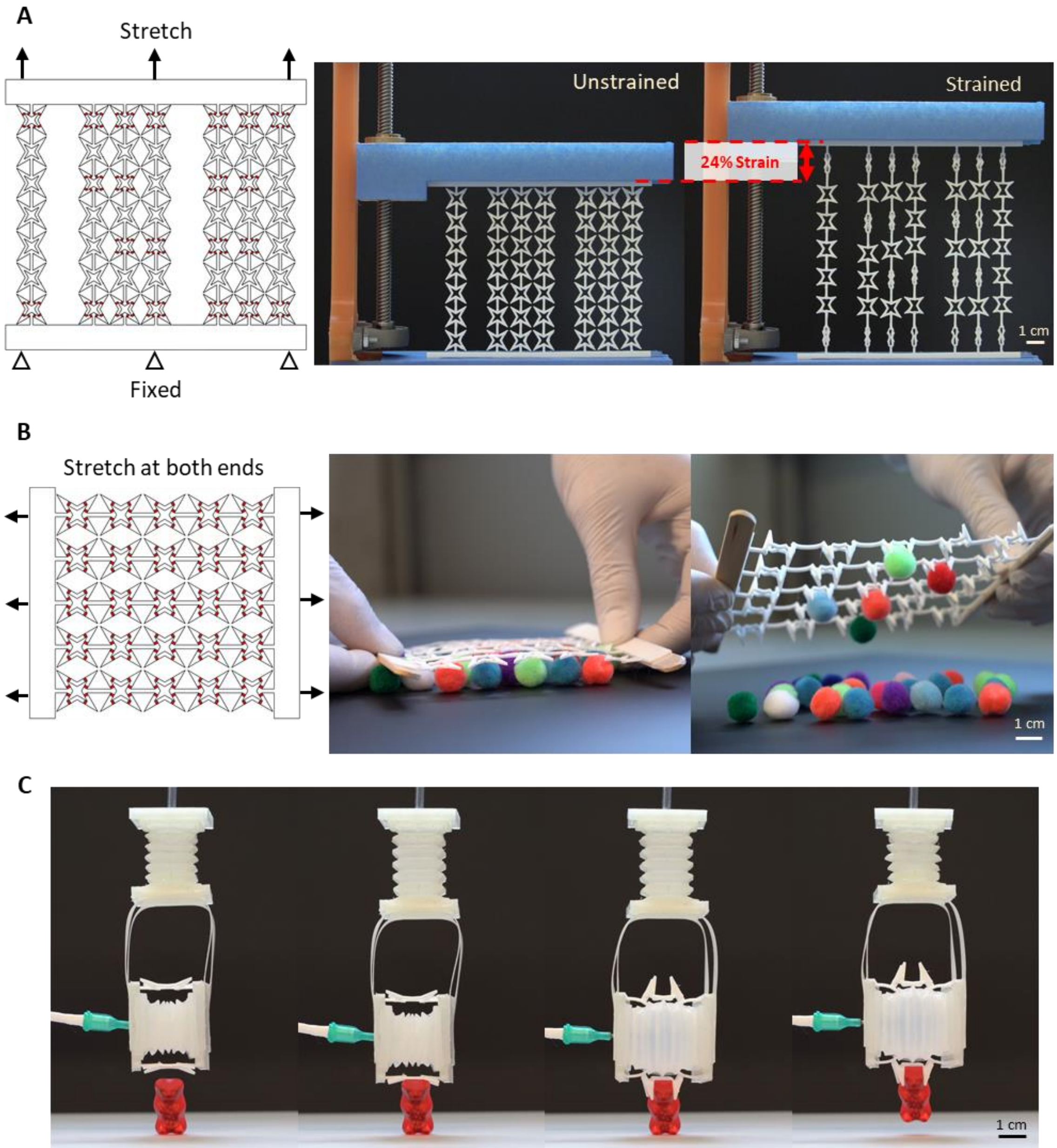

Figure 3.6. (**A**) The MAS was designed to reveal numbers "1 2 3" by selectively actuating the interconnected star array at discrete locations once uniaxial strain was applied. (**B**) A MAS was designed for large area gripping of multiple soft fur balls (~15 mm diameter) by applying uniaxial strain at the vertical edges. (**C**) A single MAS unit star used for gripping a gummy bear (~4 g). The soft crane includes two soft, linear, accordion pneumatic actuators.
Uniaxial strain is applied to the single gripper by the expansion of the soft actuator.

raising and lowering of the MAS soft robotic claw (Figure 3.7). The demonstration successfully validated that the MAS claw could lift a gummy bear that weighs ~ 4g.

3.3 Materials and Methods

3.3.1 3D printing of MAS

All single star geometries and interconnected arrays were fabricated using an Ultimaker 3, which is a commercial filament deposition modeling (FDM) 3D printer. Polyurethane thermoplastic (TPU 95A) filament (Dynamism Inc.) was used to 3D-print all of the star geometries and arrays. The geometries were designed in Autodesk Fusion 360 (2018). The 3D models (.stl) of the star geometries and all interconnected arrays were loaded in Ultimaker Cura 3.3 and fed to the 3D printer for fabrication.

3.3.2 Tensile and Tensile Cyclic Testing of MAS

Tensile and cyclic tests of the star geometry were performed by mounting each star unit cell in a Test Resource 150R load frame equipped with a 10 N load cell. The load frame was commanded to stretch the star geometry along the direction of its longitudinal axis from 0 until failure at a constant applied strain rate of 2 mm/min while simultaneously recording load and displacement. On the other hand, the reversibility of the MAS star geometry was characterized by subjecting star geometries (*i.e.,* 1 mm thick and with a normalized notch depth of h/t = 2/3) to a 20-cycle tensile load pattern to a maximum strain of 37%. Applied strain rate was fixed at 2 mm/min, while load, displacement, and time were recorded.

3.3.3 Assembly of the Soft Claw Crane

The accordion-like, soft, linear actuators were made by pouring FX-Pro elastomer (Smooth-On Inc.) into a customized, 3D-printed, three-piece polylactic acid (PLA) mold. The inside of the hollow actuator resembled the outer, accordion-like shape. The open end of the soft actuator was sealed with additional FX-Pro elastomer, making the actuator airtight. Two 3D-printed PLA caps with slits to fit the two, star unit cells were also printed and mounted

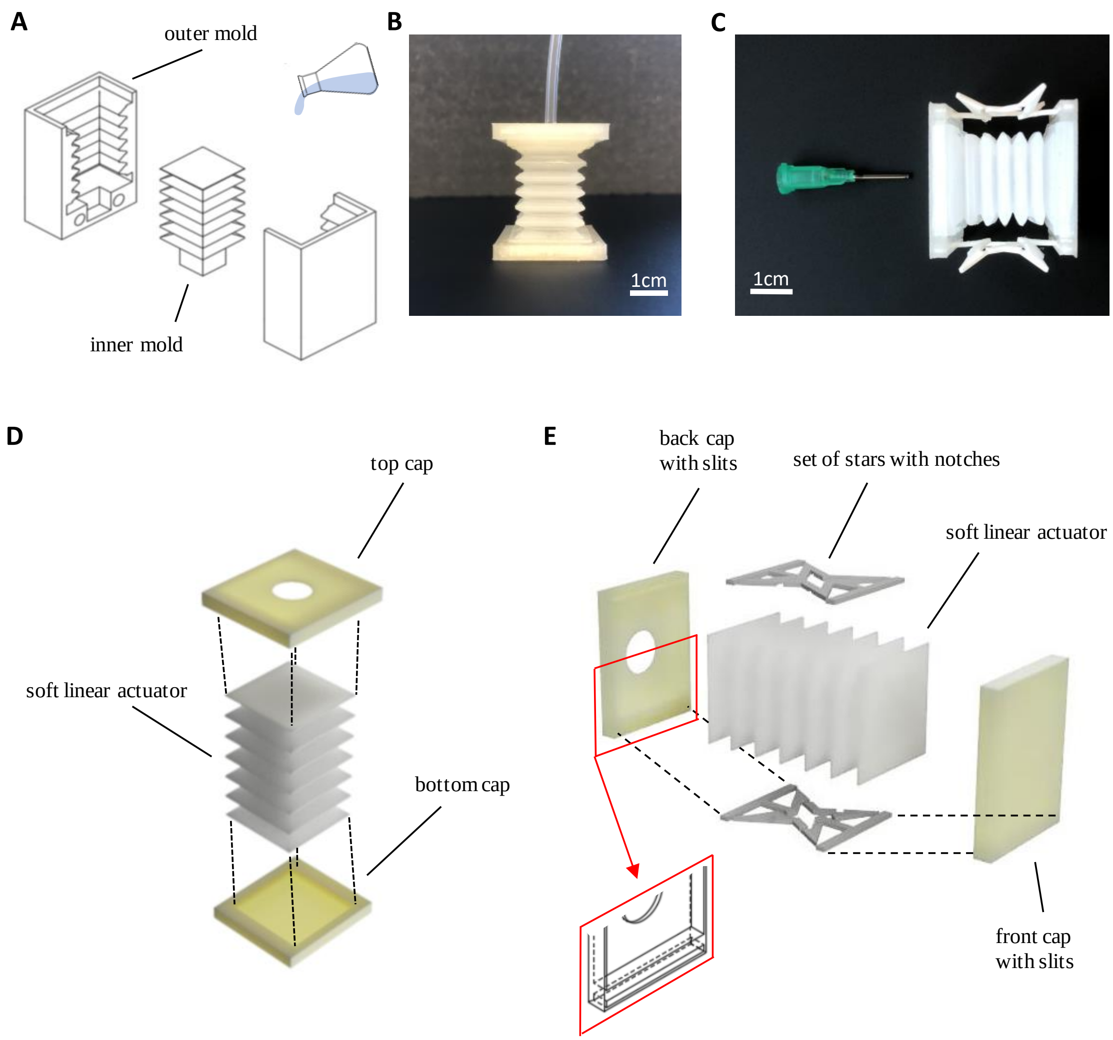

Figure 3.7. (**A**) Schematic (slanted view) of the 3D printed mold for the making of the actuator. The silicone-based elastomer is poured into the mold. (**B-C**) Picture of the assembled top actuator with tubing for pneumatic actuation and horizontal actuator for gripping with a needle for pneumatic actuation. (**D-E**) A rendering of the assembly process of the top, soft linear actuator for lowering/raising the claw crane and the bottom, soft actuator for gripping.

onto the bottom soft accordion-like actuator of the “soft crane”. The star geometries utilized as grippers were scaled up 25% in comparison to the ones used for tensile tests and analysis of the deformation mechanism. The stars were inserted in the caps slits and glued with epoxy (Gorilla Glue). An 18 gauge syringe needle was inserted in the airtight bottom actuator and sealed with additional FX-Pro elastomer to avoid any leaks. The two actuators were connected by means of a 3D-printed TPU 95A strip.

3.4 Summary

In conclusion, this Chapter presents a multifunctional active skin for programmable, reversible, rapid, and on-demand texture morphing that is actuated by applied in-plane tensile strains. The MAS leverages buckling-induced instabilities in the form of notches introduced at judicious locations in a star geometry. The optimal notch depth and substrate thickness combination of MAS were found by characterizing their deformation mechanism and the mechanical response of unit star geometries subjected to uniaxial tensile loading.

In addition, the MAS was fabricated using a commercial-off-the-shelf benchtop 3D printer, thereby further demonstrating the effectiveness of a simplified design methodology. The design approach followed in the making of the MAS presented herein can be extended to a multitude of existing architected geometries, enlarging their field of applications and hence their multifunctionality. Further developments of the MAS aim at deriving an inverse design methodology to inform placements of geometrical instabilities that can reliably produce desirable system shape morphing.

Chapter 3 is coauthored with Park, Yujin and Loh, Kenneth J. The thesis author was the primary author of this chapter.

CHAPTER 4. EIT BACKGROUND

4.1 Introduction

EIT is a soft-field imaging technique through which the electrical conductivity distribution (σ) of a predefined sensing domain (Ω) is reconstructed from a limited number of boundary voltage measurements [78]. First introduced in the 1980s as a medical imaging technique that differentiated itself from X-ray computed tomography for not employing any form of ionizing radiation, EIT remains, even today, a highly reliable technique with its implementation in a variety of fields including SHM and nondestructive evaluation (NDE) [79, 80]. In SHM and NDE, EIT applications have been mainly focused on imaging large-area, continuous structures through the application of conductive coatings and paints [81-84]. Yet, to the best of the author's knowledge, no studies have coupled EIT with materials in which architecture and geometry are non-continuous in order to address the limitations observed in previously reported "sensing skins" [85]. Below, an overview of the EIT algorithm to obtain tomographic data from a non-continuous, architected, conductive geometry is given.

In general, a set of boundary electrodes are placed around Ω. EIT interrogation entails selecting a pair of electrodes for current injection and ground, while the voltage drops across all remaining pairs of boundary electrodes are recorded. This excitation-measurement pattern is repeated for all boundary electrodes (*i.e.,* to inflict different patterns of electrical current excitations and flow through the conductive body). The entire set of measurements is then used for EIT conductivity distribution reconstruction. In essence, the EIT algorithm embodies the forward and inverse problems, which are described briefly below, and more extensive and detailed explanations can be found in the literature [79, 86].

4.2 EIT Forward Problem

The EIT forward problem seeks to calculate the voltage distribution (u) everywhere along the boundary of Ω, while σ and the current excitation patterns are known *a priori*. Mathematically, this can be described by the two-dimensional (2D) Laplace's equation:

$$\nabla\sigma \cdot (\nabla u) = 0 \tag{1}$$

Proper boundary conditions should be implemented to obtain the most accurate solution of this second-order partial differential equation [87]. The finite element method (FEM) is usually adopted to obtain an approximate solution of (1). Unlike many other investigations in which EIT is coupled with continuous conductive thin films, in this thesis, it was applied to architected, grid-like, "sensing meshes" with vertical and horizontal struts having a high aspect ratio resembling that of a 2D truss structure (further highlighted in Chapter 5). Moreover, Ω in FEM was discretized into 1D linear bar elements, resulting in a decreased computational effort for solving the forward problem due to the reduced number of points that make up the geometry.

To best evaluate the solution of (1), the appropriate boundary conditions need to be applied, which is shown in (2). The most accurate mathematical model of the forward problem, known as the complete electrode model, takes into consideration the contact impedance and the shunt resistance between boundary electrodes and Ω [87]. On the other hand, when the size of the boundary electrodes is negligible in comparison to the total area of Ω, the point electrode model is applied, thereby effectively eliminating the contact impedance (usually unknown) [87]. The boundary conditions dictated assuming an infinitesimally small point electrode are:

$$\sigma \frac{\partial u}{\partial n} = f \text{ on } \Gamma \text{ and } f = \sum_{i=1}^{M} I \delta_{x_i} \quad (2)$$

where Γ is the boundary of the conductive body Ω with a set number of M electrodes, n is the outward normal at the boundary, I is the current injected throughout EIT interrogation, and δ is the delta Dirac Delta distribution on the boundary supported at x_i. Moreover, at each EIT interrogation, the boundary condition reflecting grounding of the point electrode is also to be assigned to (1) as (u = 0). With all boundary conditions in place, a weak form of (1) is derived by multiplying it with a smooth test function (φ) and by integrating over Γ:

$$\int_{\Omega} \nabla\sigma \cdot \nabla\varphi \mathrm{d}\Omega = \int_{\Gamma} f \varphi \, \mathrm{d}\Gamma \quad (3)$$

Subsequently, the linear equations obtained from (3) are solved for the voltage distribution at each node of the architected, grid-like, body or Ω.

4.3 EIT Inverse Problem

While the EIT forward problem is solved to obtain the boundary voltage distribution, the inverse problem seeks to reconstruct the conductivity distribution of Ω using experimental boundary voltage measurements. To accomplish this, the forward problem is solved first, and a sensitivity matrix (J) is obtained. A baseline boundary voltage measurement set (V_b) is collected as the baseline. Then, to obtain the conductivity distribution corresponding to a new state (*i.e.*, due to some change being applied to Ω), the EIT data acquisition system is commanded to interrogate Ω and store the corresponding set of boundary voltage responses (V_m). The change in conductivity (x) between these two states is iteratively estimated by the Landweber algorithm as shown in Table 1; here, k indicates the number of iterations. The algorithm is iterated until the error ratio (*i.e.*, $||r||^2/||V_m||^2$) reaches a value of 0.2 %.

4.4 Summary

In summary, EIT is an imaging technique that seeks to reconstruct the conductivity distributions within a body by using only a set number of boundary electrical measurements. Interrogation of the conductive body through EIT proceeds as follows. First, two boundary electrodes, one as current injection source and the other as ground, are selected while the voltage variations at all other ones is recorded. Second, the excitation-measurement process is repeated until all combinations of boundary electrodes as injection and ground have been executed. Third, the forward problem then solves for the boundary voltage distributions across nodes (or electrodes) of the conductive body. Subsequently, the inverse problem reconstructs the conductivity distribution of the interrogated body through the previously collected voltage measurements. Thus far, EIT in SHM has been applied to continuous structures. Presented above is a novel EIT algorithmic approach for a 2D truss-like structure in the form of an architected, grid-like, topology comprising of vertical and horizontal struts. The struts, having a high aspect ratio, can be subsequently approximated as 1D linear bar elements for reducing computational effort when solving the forward problem.

Table 4.1. Landweber iterative algorithm

$b = V_m - V_b;$

$\alpha = \dfrac{2}{min(\,svd[J'J])};$

$r = b;$

while $||r||^2/||V_m||^2 \geq 0.002$ and $k \leq 20{,}000$

$x = x + \alpha J'r;$

$r = b - Jx;$

$k = k + 1;$

end

CHAPTER 5. SENSING MESHES FOR SPATIAL STRAIN SENSING

5.1 Introduction

As mentioned in Chapter 1, smart structures couple the ability to capture of sensory inputs about how it interacts with the environment and the subsequent ability to react or actuate to change its behavior and performance. In Chapter 3, full control of an instability-induced actuation response was achieved through coupling of architecture, the re-entrant, auxetic star geometry, and the design criterion of geometrical imperfections of notches.

This chapter explores how the architecture of a sensing element, when coupled with EIT as a sensing and measurement modality, can overcome the limitation of current sensors and enhance the sensitivity to external inputs (*e.g.*, strain). The design criterion of the introduced "sensing mesh" relies in the patterning of a piezoresistive thin film to form a grid- or mesh-like geometry (Figure 5.1). The grid lines of the sensing mesh were designed to be of a high aspect ratio so as to resolve strain magnitudes along the length of each element but just in the direction of the longitudinal axis of that particular element. The architected geometry was fabricated by laser-cutting a continuous polyethylene terephthalate (PET) substrate. Simultaneously, a graphene nanosheets (GNS)-based nanocomposite thin film was designed, fabricated, and tested to show that it has a significantly higher strain sensitivity (or gage factor) than previously reported CNT-based thin films. This film was then deposited onto the architected PET grid-like pattern, forming a piezoresistive sensing platform. Next, sensing mesh specimens were subjected to uniaxial load tests, and EIT measurements were recorded and processed. The experimental EIT strain field results were verified by comparing them with FEM simulations.

The motivation behind sensing meshes as an innovative sensory input source for smart structures is based on the need to measure, monitor, and prevent catastrophic failure of aerospace, civil, and marine structures. To prevent these types of events from occurring in the future, SHM aims to identify and characterize damage in engineered structures for guiding appropriate interventions and failure prevention. It should be mentioned that, although structural components undergo failure when applied stress exceeds the material's yield or ultimate strength, monitoring of stress is not feasible, as this is an engineered quantity and cannot be directly sensed or monitored. Hence, strain measurements are typically used and then converted to stress based on *a priori* knowledge or assumptions of material properties (*e.g.*, by assuming linear-elastic material behavior and Hooke's law). While knowing the average stress applied to structural components is useful in terms of estimating overall load demand and structural resistance, damage (*e.g.*, cracks) can manifest as highly localized phenomena. Therefore, distributed strain measurements are beneficial for not only characterizing strain (and stress) distributions in structural components but also for identifying the presence of localized damage features.

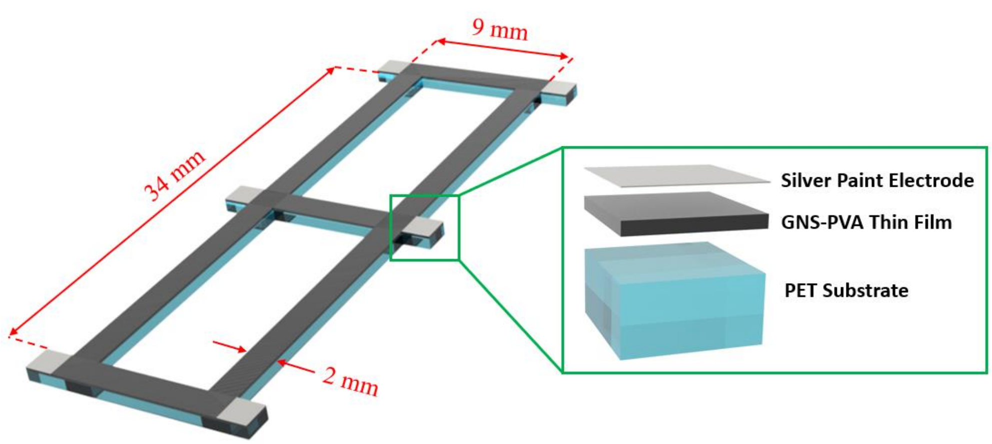

Figure 5.1. The schematic shows a 3×2 PET sensing mesh spray-coated with a graphene-based piezoresistive thin film that could be interrogated using EIT.

Moreover, the most commonly used strain transducers today are foil-based strain gages. They offer accurate and reliable measurements of strain at the location where they are installed [88]. Their implementation for large-scale infrastructure systems typically requires the use of a dense network of distributed strain sensors in order to characterize the strains (and stresses) at different locations and components. Even with a dense network installed, strain measurements are often highly distributed, and only global structural conditions can be monitored. Although strain gages can be installed at extremely high densities to characterize localized structural behavior, the complexity of installation, data acquisition demands, sensing channels required, and costs make such a strategy inefficient and prohibitive. Although in the literature other strain transduces (*e.g.*, fiber Bragg grating (FBG) strain sensors [89], polyvinylidene fluoride (PVDF) piezoelectric patch sensors [90] and soft elastomeric capacitors (SECs) [91]) have addresses the limitations of foil-based strain gages, most of these emerging technologies cannot effectively capture the strain distribution in a structure and, especially, at high spatial resolutions.

In recent years, the need for spatial strain sensing coupled with advancements in nanotechnology led to the development of piezoresistive thin film strain sensors. In particular, nanomaterials, such as CNTs and GNS, possess outstanding mechanical [92] and electrical properties [93] that can be leveraged for designing high-performance coatings with exceptional electromechanical response, especially when embedded in a polymer nano-composite matrix. For example, Hou *et al.* [81] showed that CNT-based thin films could be coupled with electrical impedance tomography (EIT) for directly sensing distributed physical, chemical, and mechanical stimuli. For EIT, the spatial conductivity (or resistivity) distributions of piezoresistive and conductive thin films were reconstructed using boundary voltage measurements. Its spatial sensing properties were validated by purposely etching portions of the film to create localized discontinuities in electrical conductivity and then using EIT to reveal these defects in the material [94]. Thereafter, Loh *et al.* [83] demonstrated that CNT-based thin films (*i.e.,* "sensing skins" [85]) could accurately resolve distributed strains, as well as residual strains in metallic plates post-impact. On the other hand, Hallaji *et al.* [82] coated a layer of conductive silver paint onto a concrete beam subjected to three-point bending and showed that the locations and extents of shear cracks were successfully captured by EIT. Despite these successes, EIT coupled with these continuous thin films cannot resolve the different components (*i.e.,* magnitudes and directions) of the strain tensor.

5.2 Experimental Details

5.2.1 Numerical Simulation Validation Study

Upon implementing the EIT algorithm (outlined in Chapter 4), a set of numerical simulations was performed for validation. An FEM of a 5×5 sensing mesh was created in ABAQUS. The model employed 55 linear truss elements to discretize the entire domain into smaller subdomains for finite element analysis. In total, 16 electrodes were modeled at the boundary of the sensing mesh. First, the electrical conductivity of the entire sensing mesh was set to 0.18 S/m (which was similar to the experimentally measured conductivity of GNS-based thin films). Second, and to inject a direct current (DC) for EIT interrogation, one electrode was selected, while its adjacent electrode was grounded. The resulting voltage drops calculated using the forward problem are shown in Figure 5.2A. In addition, a complete set of boundary voltage measurements was obtained by selecting all the pairs of two adjacent electrodes, setting one for current injection and the other as ground, and successively calculating the voltage drops between all other remaining adjacent pairs of boundary electrodes. It should be noted that the excitation and ground electrodes were excluded when computing the voltage drop to minimize the effect of noise. Thus, for N number of electrodes, this yielded N·(N-3) unique voltages. Third, artificial damage cases were defined by changing the conductivity of certain highlighted struts to 0 S/m. The non-conductive struts physically meant that those elements were broken or nonexistent (*e.g.*, due to damage). Next, the EIT forward problem was executed to calculate the boundary voltage responses corresponding to each damage case. To add realism to this numerical study, the calculated boundary voltage responses were purposely corrupted by superimposing to it a Gaussian white noise signal (*i.e.,* with an amplitude of 1% of the median of the computed voltage response). Finally, the corrupted voltage data were then used as inputs for solving the EIT inverse problem and to reconstruct the conductivity distribution of the sensing mesh. The trend of convergence of Landweber algorithm and the number of iterations needed to achieve the specified threshold limit (*i.e.*, 0.2%) is shown in Figure 5.2B.

5.2.2 Nanocomposite Thin Film Design and Specimen Preparation

Previous work by Mortensen *et al.* [95] showed that spray-coated multi-walled carbon nanotube/latex thin films possessed electromechanical properties that were sensitive to applied strains. However, its gage factor (G) was only 0.77 ± 0.02, which is lower than most conventional foil-based strain gages ($G \sim 2$). As mentioned earlier, one of the objectives of this study is to design a sensing mesh that could accurately resolve strain fields in large structural surfaces. In order to maximize signal-to-noise ratio and to enable the detection of small changes in strains, the strain sensitivity (or G) of the thin film should be high.

Thus, this study leveraged graphene nanosheets for designing high-performance thin film strain sensors. The GNS used was synthesized using a water-assisted liquid-phase exfoliation process. Moreover, film fabrication through spray coating was implemented as such fabrication methodology was deemed more suitable for large-scale implementations of this technology. To prepare the sprayable ink, a 5 wt.% poly(vinyl alcohol) (PVA) aqueous solution was used as the surfactant for dispersing GNS. The PVA solution was made by slowly adding amorphous PVA powder (Sigma-Aldrich) to boiling deionized water. A magnetic

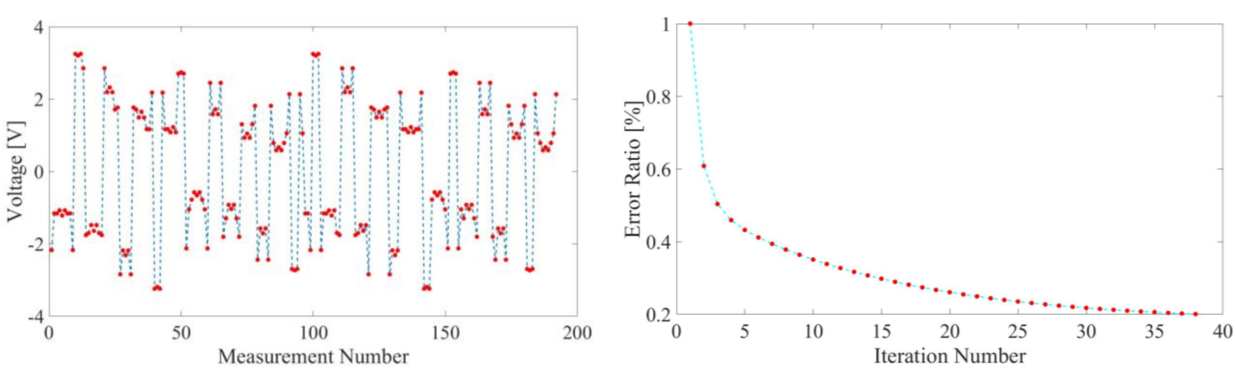

Figure 5.2. (**A**) The boundary voltage responses of the simulated sensing mesh (with a homogeneous conductivity distribution of 0.18 S/m) is plotted with respect to the measurement number when the sensing mesh was excited with a direct current of 1 mA. (**B**) A convergence plot of the Landweber iterative algorithm is shown.

stirrer rotating at 300 rpm was used to fully mix and dissolve PVA until a visually clear solution was obtained. The PVA solution was then cooled to room temperature before being used to prepare 1 wt.% GNS-PVA mixtures. The GNS-PVA mixture was subjected to 1 h of high-energy probe sonication (150 W, 22 kHz running a 5-s-on/5-s-off sonication cycle) for obtaining a homogeneous GNS dispersion in PVA. The resulting dispersion or GNS-PVA ink was then directly used for spray-coating.

PET substrates were used for creating the sensing mesh specimens. First, PET sheets (216 mm × 279 mm) were cut, using a 40 W benchtop CO2 automated laser cutter (Orion Motor Tech), to form a 3×2 grid-like sensing mesh substrate (Figure 5.1). Here, the 3×2 sensing mesh pattern was sketched in AutoCAD, before it was exported to the laser cutting software LaserDRW to produce the patterned substrate. It should be mentioned that rectangular substrates were also cut for strain sensing characterization tests, which will be discussed in Section 5.3.2. Regardless of the geometry of the substrate, the GNS-PVA ink was loaded in a Paasche airbrush and spray-coated directly onto the PET cutouts (by maintaining a constant air pressure of ~ 10 psi). The sensing mesh specimens were left overnight in ambient air to dry, before colloidal silver paste (Ted Pella) and conductive thread (Adafruit) boundary electrodes were established. Silver paste was employed for affixing the conductive threads to the sensing mesh and for reducing contact impedance. A schematic illustrating the GNS-PVA sensing mesh fabrication process is shown in Figure 5.3.

5.2.3 Strain Sensing Characterization

The strain sensing properties of the GNS-PVA nanocomposite thin films were characterized by subjecting rectangular thin film specimens to cyclic tensile loads while simultaneously recording their electrical resistance, similar to the procedure reported by

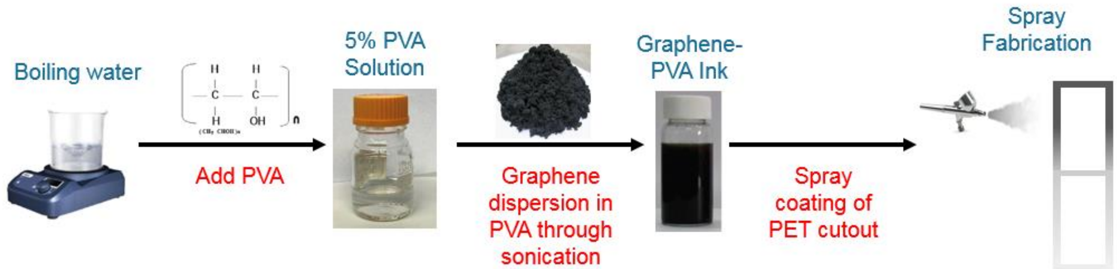

Figure 5.3. The GNS-PVA nanocomposite ink preparation and thin film fabrication process is summarized.

Mortensen *et al.* [95]. Each rectangular thin film specimen was subjected to a three-cycle tensile load pattern to a maximum value of 5,000 με at a constant rate of 15,000 με/min. The resistance of each specimen was recorded using a Keysight 34465A digital multimeter. Data was logged at a sampling rate of 2 Hz using Keysight BenchVue software.

5.2.4 Distributed Strain Field Monitoring

Testing of the distributed strain field monitoring performance of 3×2 sensing mesh specimens was performed by mounting them in a Test Resource 150R load frame equipped with a 5 N load cell. The load frame was commanded to stretch the sensing mesh along the direction of its longitudinal axis from 0 to 3,000 με at a constant applied strain rate of 1,000 με/min. After each 1,000 με increment, the load frame was manually paused, and the sensing mesh was subjected to EIT interrogations. It should be mentioned that, prior to applying any loading, a baseline EIT boundary voltage dataset was recorded. These boundary voltage measurement datasets were used as inputs to the EIT inverse problem for reconstructing the conductivity distribution of the sensing mesh at different strain states.

5.2.5 Sensing Mesh Numerical Simulations

To verify the accuracy of the spatial strain measurements obtained by load-testing the sensing mesh specimens, an elastic FEM analysis of the 3×2 sensing mesh was performed using ABAQUS. The sensing mesh was modelled as a linear-elastic substrate with a Young's Modulus and Poisson's ratio of PET being 2 GPa and 0.44, respectively. The model was discretized into 148 plane stress, bi-linear, quadrilateral elements, as shown in Figure 5.4A. The boundary conditions applied to the model consisted of pinned, non-displacing bottom-edge struts and displacing, loaded top-edge struts (Figure 5.4B). Similar to the experimental procedure discussed in Section 5.2.4, the model was strained from 0 to 3,000 με. For the 1,000, 2,000, and 3,000 με strain-states investigated, the strains along all the vertical struts (*i.e.*, V1 to V4) and horizontal struts (*i.e.*, H1 to H3) (Figure 5.4A) were extracted from the simulation results. The experimentally measured strain responses at these struts of interest (for all three strain states considered) were compared to the FEM results for verification.

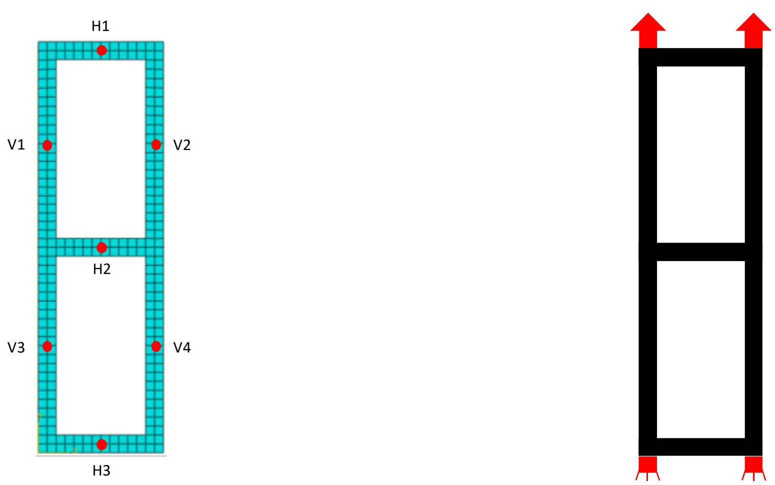

A **B**

Figure 5.4. (**A**) The discretized FEM of the simulated 3×2 sensing mesh is shown, along with the locations where strains were extracted from each strut for direct comparison with EIT experimental results. (**B**) The boundary conditions of the sensing mesh model in ABAQUS is illustrated.

5.3 Results

5.3.1 Numerical Validation of the EIT Sensing Mesh Algorithm

As mentioned in Section 5.2.1, a numerical simulation study was conducted to validate the modified EIT algorithm for detecting and localizing simulated damage in 5×5 sensing meshes (Figure 5.5A-C). Damage in the model were introduced by selectively changing the electrical conductivities (to 0 S/m) of various 1D elements in the sensing mesh (*i.e.*, to mimic the disconnection of certain struts in the sensing mesh due to, for instance, a propagating crack). The struts that were manually selected to be electrically nonconductive are highlighted in Figure 5.5A-C. Figure 5.5D-F shows the EIT sensing mesh results corresponding to the different simulated damage cases. Here, these EIT results show the changes in conductivity with respect to the undamaged sensing mesh or baseline. It can be immediately observed that the EIT results correctly identify the sensing mesh struts that were damaged. In addition, this simulation study included the effects of noise (as discussed in Section 5.2.1), and the ability for the EIT algorithm to correctly characterize damage suggests its high fidelity and promise for experimental implementations of this approach.

5.3.2 Thin Film Strain Sensing Performance

Upon fabricating the GNS-PVA thin films, they were subjected to tensile cyclic strain sensing characterization tests as described in Section 5.2.3. Figure 5.6A shows a set of representative results, where the resistance time history of the thin film is overlaid with the applied strain pattern. It is clear that the resistance of the film changes in tandem with applied strains in a stable and repeatable manner. The same dataset was processed to compute the specimen's normalized change in resistance (*i.e.*, the difference of the resistance of the film (R_i) at any given applied strain state ($\Delta\varepsilon$) with respect to its initial, unstrained, baseline resistance (R_0) and divided by R_0). Normalized change in resistance was plotted with respect to the applied strains to produce Figure 5.6B. The slope of the linear least-squares regression line is equivalent to the GNS-PVA thin film's gage factor or strain sensitivity, as shown in (2):

$$G = \frac{\Delta R / R_0}{\Delta \varepsilon} \tag{2}$$

where ΔR is $R_i - R_0$, and the numerator is normalized change in resistance. The average strain sensitivity (or G) was found to be $\sim$ 8.25, which is more than 10 times higher than the previously mentioned CNT-based thin film strain sensors [95].

5.3.3 Distributed Strain Field Monitoring Results

The spray fabrication procedure outlined in Section 5.2.2 was employed for producing 3×2 grid-like sensing mesh specimens. These specimens were mounted in a Test Resources 150R load frame and subjected to uniaxial tensile strains up to 3,000 με. Given that uniaxial loads were applied, the sensing mesh's vertical struts were expected to undergo tension, while the horizontal struts were expected to undergo compression due to Poisson's effect. After each 1,000 με interval, the 3×2 grid-like sensing mesh was interrogated using EIT, and Figure 5.7 shows the corresponding EIT reconstructed conductivity distributions. It can be immediately observed from these results that the vertical struts experienced a decrease in conductivity (or increase in resistivity), which is consistent with the strain sensing characterization test results shown in Figure 5.6A. Similarly, the horizontal struts experienced an increase in conductivity (or decrease in resistivity) due to Poisson's effect, which is also expected. In addition, the decrease in conductivity of the vertical struts and increase in conductivity of the horizontal struts were gradual and scaled with the magnitude of applied strains.

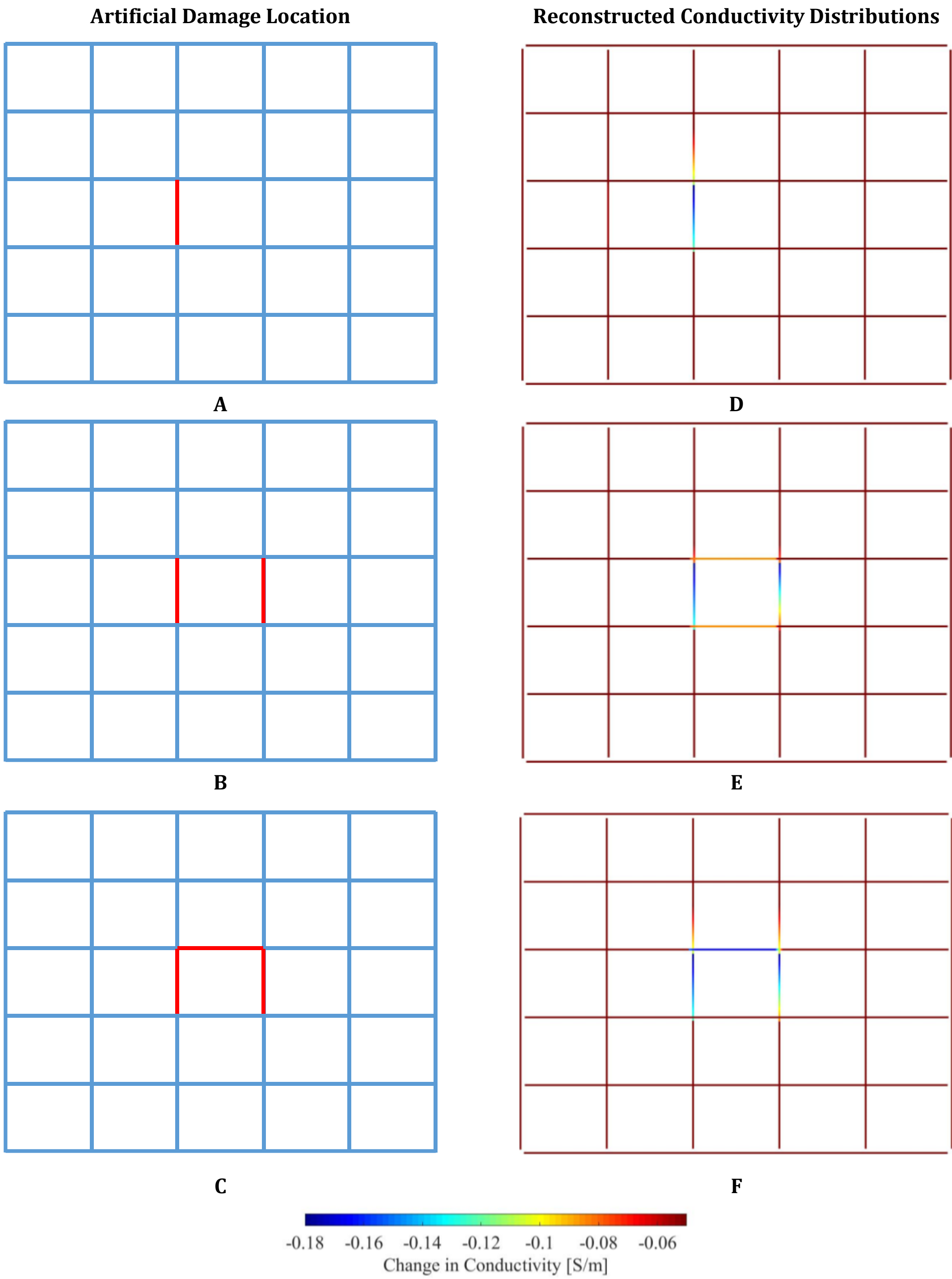

Figure 5.5. (**A-C**) show the artificial damage locations on the sensing mesh, where the red elements have a conductivity of 0 S/cm. (**D-F**) show the reconstructed conductivity distributions of the sensing mesh for each of the artificial damage cases.

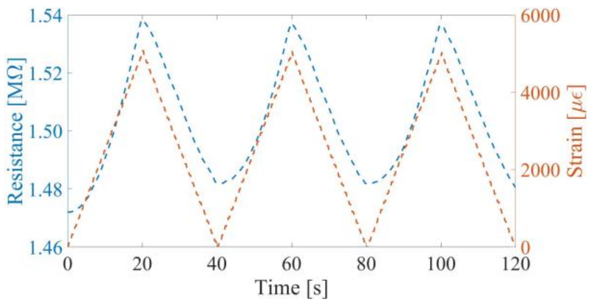

A

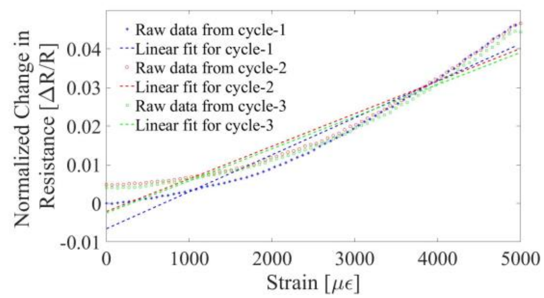

B

Figure 5.6. (**A**) The electrical resistance time history of the GNS-PVA thin film is overlaid with the corresponding applied strain time history. (**B**) The normalized change in resistance of the GNS-PVA thin film for three different loading cycles is plotted with respect to the applied strains.

5.3.4 Numerical Validation of Distributed Strain Field Monitoring

To further investigate the validity and accuracy of the EIT results, an FEM of the 3×2 sensing mesh was created in ABAQUS. As mentioned in Section 5.2.5, the model was subjected to the same loading pattern as was done experimentally in Sections 5.2.4 and 5.3.3. In the model, a total of seven points of interest, centered at each vertical (*i.e.*, V1 to V4) and horizontal (*i.e.*, H1 to H3) struts, were chosen (Figure 5.4A). The strain values at these seven locations were extracted for the different strain states and compared to the EIT results. However, since the EIT results reported the conductivity distribution of the sensing mesh, these results needed to be converted to strains for comparison purposes. This was achieved by computing the average change in strain of each strut ($\Delta\varepsilon_{strut}$) using (3):

$$\Delta\varepsilon_{strut} = \frac{\Delta\sigma/\sigma_0}{G} \tag{3}$$

where the average change in conductivity ($\Delta\sigma$) of each 1D element in the mesh was divided by the initial, baseline conductivity of the unstrained sensing mesh (σ_0).

Figure 5.8 shows the simulated strains of the sensing mesh model when subjected to different magnitudes of strains in the longitudinal or vertical direction. Here, ε_{11} (Figure 5.8A-C) corresponds to strains in the horizontal direction, while ε_{22} (Figure 5.8D-F) is strains in the vertical direction. First, the behavior of the experimental EIT results (Figure 5.7) matched those of numerical simulations (Figure 5.8). All vertical struts show an increase in tension, while all horizontal struts show an increase in compression when greater uniaxial tensile strains were applied to the sensing mesh model.

Second, Table 2 lists the strain values of each of the vertical (*i.e.*, V1 to V4) and horizontal (*i.e.*, H1 to H3) points of interest for both the numerical model and experimentally tested

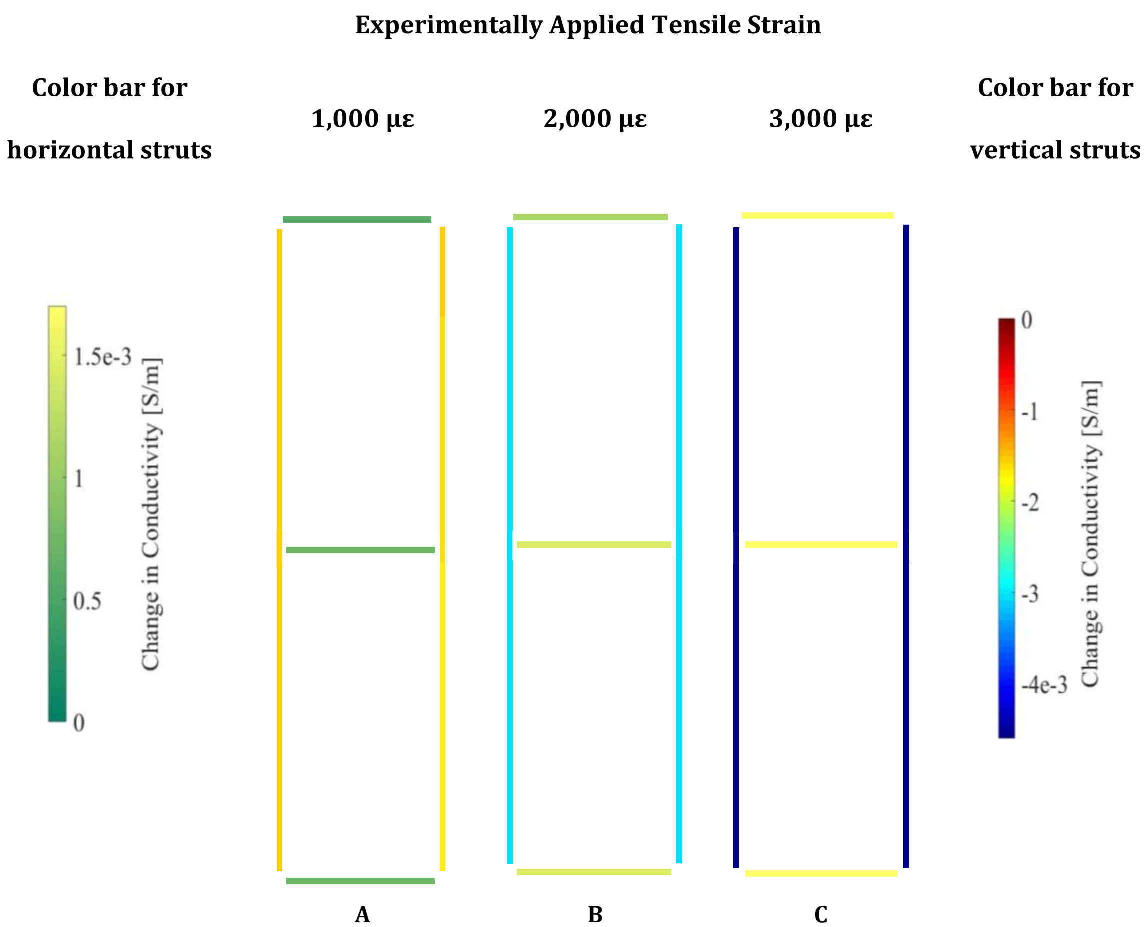

Figure 5.7. The reconstructed conductivity maps corresponding to when the sensing mesh was subjected to (**A**) 1,000, (**B**) 2,000, and (**C**) 3,000 με are shown. Vertical struts undergoing tension show a decrease in conductivity, while the horizontal struts undergoing compression, due to Poisson's effect, show an increase in conductivity.

sensing mesh specimens. Good agreement between strain calculations and experimental EIT results were found for all locations and applied strain states. The average error was found to be ~ 1.5%, which is considered to be quite small. In general, two main factors could have contributed to errors. The first is the possibility of the specimen slipping from the grips during loading and/or misalignment in the load frame, both of which could reduce the actual magnitude of the strains applied to the sensing mesh. The second is that inhomogeneities in the GNS-PVA thin film could potentially cause nonuniform strain sensitivity (*i.e.*, G) throughout the patterned film, thereby leading to errors in EIT-derived strain measurements (since only the bulk film gage factor was used for calibration). Nevertheless, the results obtained suggest that the sensing mesh functioned fairly accurately and showed tremendous promise for distributed strain field monitoring applications.

5.4 Summary

In this work, a sensing mesh was designed for distributed strain field monitoring. The sensing mesh was motivated by limitations observed in previous sensing skin studies that coupled electrical impedance tomography with strain-sensitive thin films for spatial strain sensing. It was found that continuous sensing skins, while capable at resolving locations of changes in strains (due to damage or applied loads), could not resolve the directionality of strains in different locations. Thus, the approach employed in this work was to pattern continuous films to form a grid- or mesh-like pattern. The sensing mesh pattern was

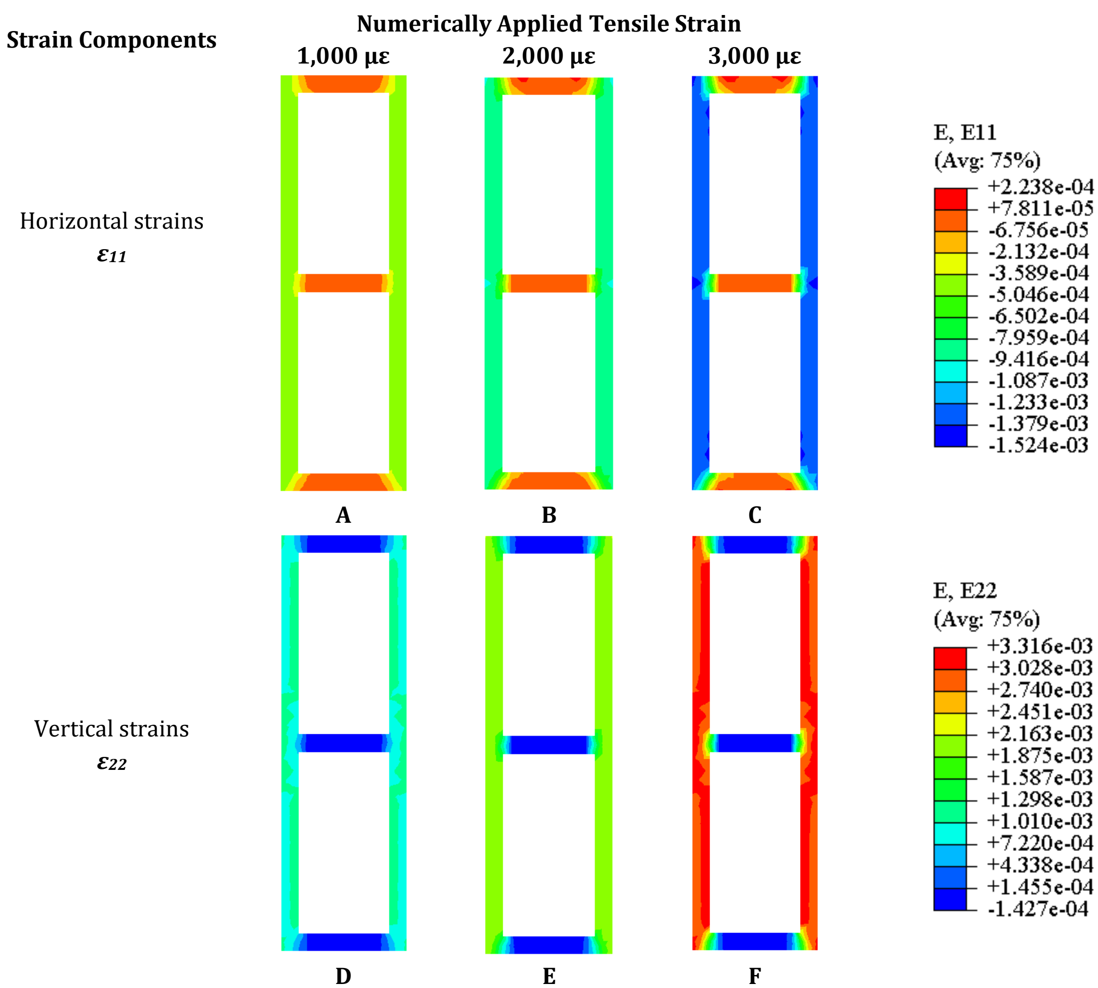

Figure 5.8. (**A-C**) show the horizontal strain distributions (ε_{11}) and (**D-F**) show the vertical strain distributions (ε_{22}) determined by subjecting the sensing mesh model in ABAQUS to three different strain states (*i.e.*, 1,000, 2,000, and 3,000 $\mu\varepsilon$).

designed such that each strut of the mesh or grid was of high aspect ratio, thereby enabling distributed sensing in each strut but limited to the direction of its length. However, to still use EIT for reconstructing the conductivity distribution of the sensing mesh, a modified EIT algorithm was first implemented. Second, the validity of the modified EIT algorithm was verified through a computational study, where arbitrary damage was introduced to a numerical model of the sensing mesh. The computed boundary voltages, after corruption with Gaussian white noise, was used as inputs to solve the EIT inverse problem to show that localized changes in conductivity could be correctly identified. With the EIT algorithm verified, a new graphene nanosheet-based thin film strain sensor with a gage factor of ~ 8.25 was fabricated and characterized. The GNS-PVA film was then used to produce 3×2 sensing mesh specimens. Sensing mesh specimens were loaded to different strain states using an electromechanical load frame, and EIT was utilized to interrogate the loaded specimens. The reconstructed conductivity distribution successfully showed the sensing mesh's ability to not only measure the magnitudes of strains but also their directionality strictly based on the locations and orientations of each strut in the mesh. Further verification of these results was performed by conducting a finite element model analysis of the sensing mesh subjected to the same strain states. Good agreement between experimental and numerical simulation results were observed. Future work will investigate the scalability of the sensing mesh by fabricating and testing larger and denser sensing mesh patterns subjected to different loading scenarios.

Chapter 5, in full, is a reprint of the material as it appears in Large Area Distributed Strain Monitoring Using Patterned Nanocomposite Sensing Meshes, Proc. SPIE - Sensors and

Table 5.1. EIT results at different sensing mesh locations (*i.e.*, V1 to V4 and H1 to H3) are compared to FEM results.

		Location	EIT Result	FEM Result	% Error
1,000 με	**Vertical Struts**	**V1**	9.93E-04	1.015E-03	1.24
		V2	1.012E-03	1.024E-03	1.23
		V3	9.91E-04	1.004E-03	1.29
		V4	1.011E-03	1.012E-03	0.17
	Horizontal Struts	**H1**	3.64E-04	3.72E-04	2.13
		H2	4.63E-04	4.73E-04	2.21
		H3	4.63E-04	4.74E-04	2.46
2,000 με	**Vertical Struts**	**V1**	1.987E-03	2.013E-03	1.31
		V2	1.982E-03	2.006E-03	1.21
		V3	1.982E-03	2.006E-03	1.21
		V4	2.021E-03	2.013E-03	0.42
	Horizontal Struts	**H1**	7.28E-04	7.44E-04	2.21
		H2	9.26E-04	9.46E-04	2.23
		H3	9.26E-04	9.49E-04	2.51
3,000 με	**Vertical Struts**	**V1**	2.983E-03	3.02E-03	1.35
		V2	3.004E-03	3.0460E-03	1.41
		V3	2.977E-03	3.0103E-03	1.11
		V4	3.000E-03	3.038E-03	1.28
	Horizontal Struts	**H1**	1.093E-03	1.116E-03	2.11
		H2	1.388E-03	1.421E-03	2.33
		H3	1.388E-03	1.422E-03	2.41

Smart Structures Technologies for Civil, Mechanical, and Aerospace Systems, 2019. The thesis author was the primary investigator of this paper.

CHAPTER 6. CONCLUSIONS

6.1 Summary

This thesis explored the geometrical criteria that guide the design of architected materials as a medium to create novel actuators and sensors. The motivation for this study was based on today's urgent need for smart and resilient structures that is capable of acquiring sensory inputs from its surroundings and then responding accordingly with an actuation response. Within the context of smart structures, architected materials have been growing in popularity within the scientific community as these represent a versatile engineered platform to achieve functionalities that go beyond those inherent to the materials that constitute them.

Mechanical metamaterials are a subset of architected materials and rely on the ingenious design of elemental unit cells to harvests deformations, stresses, nonlinear responses, instabilities, and mechanical energy of the bulk material in order to achieve desired performances [25]. Most often, as the complexity of architectures increases, so do the embedded functionalities that mechanical metamaterials exhibit. New and advanced fabrication methodologies such as AM have made it possible to reach close to unlimited design freedom and manufacturing feasibility of complex mechanical metamaterials. Chapter 2 of this thesis introduced the most prominent light- and extrusion-based manufacturing techniques, which are then utilized in the fabrication of MAS.

3D printing, the leading additive manufacturing technique today, is paramount to the MAS, new skin-like actuators for surface morphing, in which their functionalities are solely given through architecture design criteria. Presented in Chapter 3, the MAS were conceptualized as a multifunctional skin for programmable, reversible, rapid, and on-demand texture morphing that is actuated by in-plane tensile strains. The MAS leveraged buckling-induced instabilities in the form of notches introduced at judicious locations in a star geometry. The optimal notch depth and substrate thickness combination of MAS were found by characterizing their deformation mechanism and the mechanical response of unit star geometries subjected to uniaxial tensile loading. Moreover, fabrication of the MAS using a commercial-off-the-shelf benchtop 3D printer, further demonstrated the effectiveness of a simplified design methodology.

Shifting away from the actuation domain of innovative smart structures, Chapter 4 transitioned to give an overview of EIT. EIT is a soft-field imaging technique through which the electrical conductivity distribution of a predefined sensing domain (or body) is reconstructed from a limited number of boundary voltage measurements. Here, an innovative EIT algorithm that benefits from the geometrical criterion of grid-like patterning of 2D thin film sensors was introduced, resulting in enhanced performance (*i.e.*, the ability to map strain fields and is presented in Chapter 5).

Finally, Chapter 5 extrapolated the design criterion of long, high aspect ratio trusses that bend uniformly under load in 3D architected lattice structures to replicate it as 3×2, 2D, mesh-like pattern with high aspect ratio struts. Coupling of the mesh architecture with a highly piezoresistive graphene-based coating (with gage factor of ~8.25) enabled each grid element to sense distributed strain along its length and direction, resembling a network of interconnected linear strain gauges. Good agreement between the experimental tests and numerical simulations were observed, thereby demonstrating the potential of this technology for distributed strain field monitoring.

6.2 Future Work

For the MAS proposed in this research, the short-term goal will consist of enlarging its multifunctional performance attributes. To do so, a more thorough study of the deformation mechanism through FEM will be performed to attain a more complete understanding of how the geometrical placement of notches, as well as their width, length and shape, impact the instability-induced out-of-plane deformations. This will result in a more controlled surface morphing actuation response, to be tailored accordingly to the MAS's specific end use. Next, combining the architecture with a multi-material design approach will enable us to expand even further the multifunctionality of MAS. For example, coupling with smart materials (*i.e.*, shape memory polymers and dielectric elastomers) or materials with physical responsiveness (*i.e.*, light, pH, and temperature, as well as electrical and magnetic field) will induce new stimuli-responsive mechanical behaviors, requiring fine-tuning of the geometry according to its functionality. Furthermore, the long-term research goals for the MAS will consist of developing an inverse design methodology to inform placements of geometrical instabilities that can reliably produce desirable system shape morphing, which is not only applicable to the star geometry but also to the multitude of 2D architected geometries previously investigated and reported in the literature.

For the sensing mesh work presented, the short-term vision will consist of reaching field deployment. First, a materials-based investigation will be performed to eliminate the rigid PET substrate, leaving a freestanding graphene-based thin film with improved sensitivity to deformations and applied strains. Next, to further enhance sensitivity, a more complex geometry to pattern the thin film will be investigated. For example, implementing auxetic geometries that respond to axial deformation with increased orthogonal strains throughout the struts of the mesh could be implemented. Finally, thorough laboratory tests will be conducted to identify the effects on the sensitivity that environmental factors present in field conditions (*e.g.*, heat, humidity, and UV-exposure) could have on the mesh. Such environmental effects will need to be addressed or taken into account as baseline factors to enhance their performance for a wider variety of field conditions.

REFERENCES

1. Cao, W., H.H. Cudney, and R. Waser, *Smart materials and structures.* Proceedings of the National Academy of Sciences, 1999. **96**(15): p. 8330-8331.

2. McGrath, M.J., C.N. Scanaill, and D. Nafus, *Sensor technologies: healthcare, wellness and environmental applications*. 2014: Apress.

3. Boldea, I. and S.A. Nasar, *Linear electric actuators and generators.* IEEE Transactions on Energy Conversion, 1999. **14**(3): p. 712-717.

4. Nespoli, A., S. Besseghini, S. Pittaccio, E. Villa, and S. Viscuso, *The high potential of shape memory alloys in developing miniature mechanical devices: A review on shape memory alloy mini-actuators.* Sensors and Actuators A: Physical, 2010. **158**(1): p. 149-160.

5. Barbarino, S., O. Bilgen, R.M. Ajaj, M.I. Friswell, and D.J. Inman, *A review of morphing aircraft.* Journal of intelligent material systems and structures, 2011. **22**(9): p. 823-877.

6. Sun, J., Q. Guan, Y. Liu, and J. Leng, *Morphing aircraft based on smart materials and structures: A state-of-the-art review.* Journal of Intelligent material systems and structures, 2016. **27**(17): p. 2289-2312.

7. Hanlon, R., *Cephalopod dynamic camouflage.* Current Biology, 2007. **17**(11): p. R400-R404.

8. Sullivan, T.N., B. Wang, H.D. Espinosa, and M.A. Meyers, *Extreme lightweight structures: avian feathers and bones.* Materials Today, 2017. **20**(7): p. 377-391.

9. Lee, N., M. Horstemeyer, H. Rhee, B. Nabors, J. Liao, and L.N. Williams, *Hierarchical multiscale structure–property relationships of the red-bellied woodpecker (Melanerpes carolinus) beak.* Journal of The Royal Society Interface, 2014. **11**(96): p. 20140274.

10. May, P.R., J.M. Fuster, J. Haber, and A. Hirschman, *Woodpecker drilling behavior: an endorsement of the rotational theory of impact brain injury.* Archives of Neurology, 1979. **36**(6): p. 370-373.

11. Yoon, S.-H. and S. Park, *A mechanical analysis of woodpecker drumming and its application to shock-absorbing systems.* Bioinspiration & Biomimetics, 2011. **6**(1): p. 016003.

12. Weiss, I.M. and H.O. Kirchner, *The peacock's train (Pavo cristatus and Pavo cristatus mut. alba) I. structure, mechanics, and chemistry of the tail feather coverts.* Journal of Experimental Zoology Part A: Ecological Genetics and Physiology, 2010. **313**(10): p. 690-703.

13. Schlecht, S.H., E.M. Bigelow, and K.J. Jepsen, *Mapping the natural variation in whole bone stiffness and strength across skeletal sites.* Bone, 2014. **67**: p. 15-22.

14. Schaedler, T.A. and W.B. Carter, *Architected cellular materials.* Annual Review of Materials Research, 2016. **46**: p. 187-210.

15. SPADACCINI, C. *Mechanical metamaterials: design, fabrication, and performance*. in *Frontiers of Engineering: Reports on Leading-Edge Engineering from the 2015 Symposium*. 2016. National Academies Press.

16. Bose, J.C., *On the rotation of plane of polarisation of electric wave by a twisted structure.* Proceedings of the Royal Society of London, 1898. **63**(389-400): p. 146-152.

17. Valdevit, L., K. Bertoldi, J. Guest, and C. Spadaccini, *Introduction. Journal of Materials Research.* 2018. p. 241-146.

18. Smith, D.R., J.B. Pendry, and M.C. Wiltshire, *Metamaterials and negative refractive index.* Science, 2004. **305**(5685): p. 788-792.

19. Shalaev, V.M., *Optical negative-index metamaterials.* Nature photonics, 2007. **1**(1): p. 41.

20. Pendry, J.B., *Negative refraction makes a perfect lens.* Physical review letters, 2000. **85**(18): p. 3966.

21. Taubner, T., D. Korobkin, Y. Urzhumov, G. Shvets, and R. Hillenbrand, *Near-field microscopy through a SiC superlens.* Science, 2006. **313**(5793): p. 1595-1595.

22. Schurig, D., J. Mock, B. Justice, S.A. Cummer, J.B. Pendry, A. Starr, and D. Smith, *Metamaterial electromagnetic cloak at microwave frequencies.* Science, 2006. **314**(5801): p. 977-980.

23. Kushwaha, M.S., P. Halevi, L. Dobrzynski, and B. Djafari-Rouhani, *Acoustic band structure of periodic elastic composites.* Physical review letters, 1993. **71**(13): p. 2022.

24. Liu, Z., X. Zhang, Y. Mao, Y. Zhu, Z. Yang, C.T. Chan, and P. Sheng, *Locally resonant sonic materials.* science, 2000. **289**(5485): p. 1734-1736.

25. Bertoldi, K., V. Vitelli, J. Christensen, and M. van Hecke, *Flexible mechanical metamaterials.* Nature Reviews Materials, 2017. **2**(11): p. 17066.

26. Evans, K.E., M. Nkansah, I. Hutchinson, and S. Rogers, *Molecular network design.* Nature, 1991. **353**(6340): p. 124.

27. Grima, J.N. and K.E. Evans, *Auxetic behavior from rotating squares.* Journal of Materials Science Letters, 2000. **19**(17): p. 1563-1565.

28. Lakes, R., *Foam structures with a negative Poisson's ratio.* Science, 1987. **235**: p. 1038-1041.

29. Jiang, Y., Z. Liu, N. Matsuhisa, D. Qi, W.R. Leow, H. Yang, J. Yu, G. Chen, Y. Liu, and C. Wan, *Auxetic mechanical metamaterials to enhance sensitivity of stretchable strain sensors.* Advanced Materials, 2018. **30**(12): p. 1706589.

30. Yu, X., J. Zhou, H. Liang, Z. Jiang, and L. Wu, *Mechanical metamaterials associated with stiffness, rigidity and compressibility: A brief review.* Progress in Materials Science, 2018. **94**: p. 114-173.

31. Lim, T.-C., *Negative thermal expansion structures constructed from positive thermal expansion trusses.* Journal of Materials Science, 2012. **47**(1): p. 368-373.

32. Ghaedizadeh, A., J. Shen, X. Ren, and Y.M. Xie, *Designing composites with negative linear compressibility.* Materials & Design, 2017. **131**: p. 343-357.

33. Aliev, A.E., J. Oh, M.E. Kozlov, A.A. Kuznetsov, S. Fang, A.F. Fonseca, R. Ovalle, M.D. Lima, M.H. Haque, and Y.N. Gartstein, *Giant-stroke, superelastic carbon nanotube aerogel muscles.* science, 2009. **323**(5921): p. 1575-1578.

34. Baughman, R.H., S. Stafström, C. Cui, and S.O. Dantas, *Materials with negative compressibilities in one or more dimensions.* Science, 1998. **279**(5356): p. 1522-1524.

35. Deshpande, V., M. Ashby, and N. Fleck, *Foam topology: bending versus stretching dominated architectures.* Acta materialia, 2001. **49**(6): p. 1035-1040.

36. Thomson, W., *LXIII. On the division of space with minimum partitional area.* The London, Edinburgh, and Dublin Philosophical Magazine and Journal of Science, 1887. **24**(151): p. 503-514.

37. Schaedler, T.A., A.J. Jacobsen, A. Torrents, A.E. Sorensen, J. Lian, J.R. Greer, L. Valdevit, and W.B. Carter, *Ultralight metallic microlattices.* Science, 2011. **334**(6058): p. 962-965.

38. Bauer, J., S. Hengsbach, I. Tesari, R. Schwaiger, and O. Kraft, *High-strength cellular ceramic composites with 3D microarchitecture.* Proceedings of the National Academy of Sciences, 2014. **111**(7): p. 2453-2458.

39. Zhu, C., T.Y.-J. Han, E.B. Duoss, A.M. Golobic, J.D. Kuntz, C.M. Spadaccini, and M.A. Worsley, *Highly compressible 3D periodic graphene aerogel microlattices.* Nature communications, 2015. **6**: p. 6962.

40. Hibbeler, R.C. and S. Fan, *Statics and mechanics of materials*. Vol. 2. 2004: Prentice Hall Singapore.

41. Hayes, A.M., A. Wang, B.M. Dempsey, and D.L. McDowell, *Mechanics of linear cellular alloys.* Mechanics of Materials, 2004. **36**(8): p. 691-713.

42. Mullin, T., S. Deschanel, K. Bertoldi, and M.C. Boyce, *Pattern transformation triggered by deformation.* Physical review letters, 2007. **99**(8): p. 084301.

43. Liu, J., T. Gu, S. Shan, S.H. Kang, J.C. Weaver, and K. Bertoldi, *Harnessing buckling to design architected materials that exhibit effective negative swelling.* Advanced Materials, 2016. **28**(31): p. 6619-6624.

44. Wang, P., J. Shim, and K. Bertoldi, *Effects of geometric and material nonlinearities on tunable band gaps and low-frequency directionality of phononic crystals.* Physical Review B, 2013. **88**(1): p. 014304.

45. Rafsanjani, A., Y. Zhang, B. Liu, S.M. Rubinstein, and K. Bertoldi, *Kirigami skins make a simple soft actuator crawl.* Science Robotics, 2018. **3**(15): p. eaar7555.

46. Chen, T., O.R. Bilal, K. Shea, and C. Daraio, *Harnessing bistability for directional propulsion of soft, untethered robots.* Proceedings of the National Academy of Sciences, 2018. **115**(22): p. 5698-5702.

47. Cazottes, P., A. Fernandes, J. Pouget, and M. Hafez, *Bistable buckled beam: modeling of actuating force and experimental validations.* Journal of Mechanical Design, 2009. **131**(10): p. 101001.

48. Shan, S., S.H. Kang, J.R. Raney, P. Wang, L. Fang, F. Candido, J.A. Lewis, and K. Bertoldi, *Multistable architected materials for trapping elastic strain energy.* Advanced Materials, 2015. **27**(29): p. 4296-4301.

49. Meza, L.R., S. Das, and J.R. Greer, *Strong, lightweight, and recoverable three-dimensional ceramic nanolattices.* Science, 2014. **345**(6202): p. 1322-1326.

50. Rafsanjani, A., A. Akbarzadeh, and D. Pasini, *Snapping mechanical metamaterials under tension.* Advanced Materials, 2015. **27**(39): p. 5931-5935.

51. Rafsanjani, A. and D. Pasini, *Bistable auxetic mechanical metamaterials inspired by ancient geometric motifs.* Extreme Mechanics Letters, 2016. **9**: p. 291-296.

52. Grima, J.N., L. Mizzi, K.M. Azzopardi, and R. Gatt, *Auxetic perforated mechanical metamaterials with randomly oriented cuts.* Advanced materials, 2016. **28**(2): p. 385-389.

53. Celli, P., C. McMahan, B. Ramirez, A. Bauhofer, C. Naify, D. Hofmann, B. Audoly, and C. Daraio, *Shape-morphing architected sheets with non-periodic cut patterns.* Soft matter, 2018. **14**(48): p. 9744-9749.

54. Kang, S.H., S. Shan, A. Košmrlj, W.L. Noorduin, S. Shian, J.C. Weaver, D.R. Clarke, and K. Bertoldi, *Complex ordered patterns in mechanical instability induced geometrically frustrated triangular cellular structures.* Physical review letters, 2014. **112**(9): p. 098701.

55. Crump, S.S., *Apparatus and method for creating three-dimensional objects*. 1992, Google Patents.

56. Crump, S.S., *Modeling apparatus for three-dimensional objects*. 1994, Google Patents.

57. Gardan, J., *Additive manufacturing technologies: state of the art and trends.* International Journal of Production Research, 2016. **54**(10): p. 3118-3132.

58. Valdevit, L. and J. Bauer, *Fabrication of 3D micro-architected/nano-architected materials*, in *Three-Dimensional Microfabrication Using Two-photon Polymerization*. 2016, Elsevier. p. 345-373.

59. Zhang, J.X. and K. Hoshino, *Molecular Sensors and Nanodevices: Principles, Designs and Applications in Biomedical Engineering*. 2018: Academic Press.

60. Allen, J.J., G.R. Bell, A.M. Kuzirian, S.S. Velankar, and R.T. Hanlon, *Comparative morphology of changeable skin papillae in octopus and cuttlefish.* Journal of morphology, 2014. **275**(4): p. 371-390.

61. Alderson, A. and K. Alderson, *Auxetic materials.* Proceedings of the Institution of Mechanical Engineers, Part G: Journal of Aerospace Engineering, 2007. **221**(4): p. 565-575.

62. Gaspar, N., X. Ren, C.W. Smith, J. Grima, and K.E. Evans, *Novel honeycombs with auxetic behaviour.* Acta Materialia, 2005. **53**(8): p. 2439-2445.

63. Mizzi, L., K.M. Azzopardi, D. Attard, J.N. Grima, and R. Gatt, *Auxetic metamaterials exhibiting giant negative Poisson's ratios.* physica status solidi (RRL)–Rapid Research Letters, 2015. **9**(7): p. 425-430.

64. Hwang, D.-G. and M.D. Bartlett, *Tunable mechanical metamaterials through hybrid kirigami structures.* Scientific reports, 2018. **8**(1): p. 3378.

65. Wang, Q., J.A. Jackson, Q. Ge, J.B. Hopkins, C.M. Spadaccini, and N.X. Fang, *Lightweight mechanical metamaterials with tunable negative thermal expansion.* Physical review letters, 2016. **117**(17): p. 175901.

66. Nicolaou, Z.G. and A.E. Motter, *Mechanical metamaterials with negative compressibility transitions.* Nature materials, 2012. **11**(7): p. 608.

67. Zhang, H., X. Guo, J. Wu, D. Fang, and Y. Zhang, *Soft mechanical metamaterials with unusual swelling behavior and tunable stress-strain curves.* Science advances, 2018. **4**(6): p. eaar8535.

68. Yang, D., B. Mosadegh, A. Ainla, B. Lee, F. Khashai, Z. Suo, K. Bertoldi, and G.M. Whitesides, *Buckling of elastomeric beams enables actuation of soft machines.* Advanced Materials, 2015. **27**(41): p. 6323-6327.

69. Dias, M.A., M.P. McCarron, D. Rayneau-Kirkhope, P.Z. Hanakata, D.K. Campbell, H.S. Park, and D.P. Holmes, *Kirigami actuators.* Soft matter, 2017. **13**(48): p. 9087-9092.

70. Zhang, Y., Z. Yan, K. Nan, D. Xiao, Y. Liu, H. Luan, H. Fu, X. Wang, Q. Yang, and J. Wang, *A mechanically driven form of Kirigami as a route to 3D mesostructures in micro/nanomembranes.* Proceedings of the National Academy of Sciences, 2015. **112**(38): p. 11757-11764.

71. Bauhofer, A.A., S. Krödel, J. Rys, O.R. Bilal, A. Constantinescu, and C. Daraio, *Harnessing photochemical shrinkage in direct laser writing for shape morphing of polymer sheets.* Advanced Materials, 2017. **29**(42): p. 1703024.

72. Theocaris, P., G. Stavroulakis, and P. Panagiotopoulos, *Negative Poisson's ratios in composites with star-shaped inclusions: a numerical homogenization approach.* Archive of Applied Mechanics, 1997. **67**(4): p. 274-286.

73. Tang, H.-W., W.-D. Chou, and L.-W. Chen, *Wave propagation in the polymer-filled star-shaped honeycomb periodic structure.* Applied Physics A, 2017. **123**(8): p. 523.

74. Meng, J., Z. Deng, K. Zhang, X. Xu, and F. Wen, *Band gap analysis of star-shaped honeycombs with varied Poisson's ratio.* Smart Materials and Structures, 2015. **24**(9): p. 095011.

75. Chen, M., H. Jiang, H. Zhang, D. Li, and Y. Wang, *Design of an acoustic superlens using single-phase metamaterials with a star-shaped lattice structure.* Scientific reports, 2018. **8**(1): p. 1861.

76. Cantournet, S., R. Desmorat, and J. Besson, *Mullins effect and cyclic stress softening of filled elastomers by internal sliding and friction thermodynamics model.* International Journal of Solids and Structures, 2009. **46**(11-12): p. 2255-2264.

77. Lee, H.-J. and K.J. Loh, *Soft material actuation by atomization.* Smart Materials and Structures, 2018.

78. Borsic, A., E. Attardo, and R. Halter, *Multi-GPU Jacobian accelerated computing for soft-field tomography.* Physiological measurement, 2012. **33**(10): p. 1703.

79. Holder, D.S., *Electrical impedance tomography: methods, history and applications*. 2004: CRC Press.

80. Cheney, M., D. Isaacson, and J.C. Newell, *Electrical impedance tomography.* SIAM review, 1999. **41**(1): p. 85-101.

81. Hou, T.-C., K.J. Loh, and J.P. Lynch, *Spatial conductivity mapping of carbon nanotube composite thin films by electrical impedance tomography for sensing applications.* Nanotechnology, 2007. **18**(31): p. 315501.

82. Hallaji, M., A. Seppänen, and M. Pour-Ghaz, *Electrical impedance tomography-based sensing skin for quantitative imaging of damage in concrete.* Smart Materials and Structures, 2014. **23**(8): p. 085001.

83. Loh, K.J., T.-C. Hou, J.P. Lynch, and N.A. Kotov, *Carbon nanotube sensing skins for spatial strain and impact damage identification.* Journal of nondestructive evaluation, 2009. **28**(1): p. 9-25.

84. Gupta, S., J.G. Gonzalez, and K.J. Loh, *Self-sensing concrete enabled by nano-engineered cement-aggregate interfaces.* Structural Health Monitoring, 2017. **16**(3): p. 309-323.

85. Loh, K.J. and F. Azhari, *Recent advances in skin-inspired sensors enabled by nanotechnology.* JOM, 2012. **64**(7): p. 793-801.

86. Borcea, L., *Electrical impedance tomography.* Inverse problems, 2002. **18**(6): p. R99.

87. Hanke, M., B. Harrach, and N. Hyvönen, *Justification of point electrode models in electrical impedance tomography.* Mathematical Models and Methods in Applied Sciences, 2011. **21**(06): p. 1395-1413.

88. Webb, G., P. Vardanega, and C. Middleton, *Categories of SHM deployments: technologies and capabilities.* Journal of Bridge Engineering, 2014. **20**(11): p. 04014118.

89. Morey, W.W., J.R. Dunphy, and G. Meltz, *Multiplexing fiber Bragg grating sensors.* Fiber & Integrated Optics, 1991. **10**(4): p. 351-360.

90. Guzman, E., J. Cugnoni, T. Gmür, P. Bonhôte, and A. Schorderet, *Survivability of integrated PVDF film sensors to accelerated ageing conditions in aeronautical/aerospace structures.* Smart materials and structures, 2013. **22**(6): p. 065020.

91. Downey, A., S. Laflamme, and F. Ubertini, *Reconstruction of in-plane strain maps using hybrid dense sensor network composed of sensing skin.* Measurement Science and Technology, 2016. **27**(12): p. 124016.

92. Treacy, M.J., T. Ebbesen, and J. Gibson, *Exceptionally high Young's modulus observed for individual carbon nanotubes.* nature, 1996. **381**(6584): p. 678.

93. Neto, A.C., F. Guinea, N.M. Peres, K.S. Novoselov, and A.K. Geim, *The electronic properties of graphene.* Reviews of modern physics, 2009. **81**(1): p. 109.

94. Loh, K.J.-H., *Development of Multifunctional Carbon Nanotube Nanocomposite Sensors for Structural Health Monitoring.* 2008.

95. Mortensen, L.P., D.H. Ryu, Y.J. Zhao, and K.J. Loh. *Rapid assembly of multifunctional thin film sensors for wind turbine blade monitoring*. in *Key Engineering Materials*. 2013. Trans Tech Publ.